Czech Technical University in Prague

Faculty of Electrical Engineering

Doctoral Thesis

August 2013

RNDr. Ivan Hirka

Czech Technical University in Prague

Faculty of Electrical Engineering
Department of Physics

NUMERICAL MODELLING OF PROCESSES IN THERMAL PLASMA REACTOR

Doctoral Thesis

RNDr. Ivan Hirka

Prague, August 2013

Ph.D. Programme: Electrical Engineering and Information Technology
Branch of study: *Plasma Physics*

Supervisor: *Doc.RNDr. Milan Hrabovsky, CSc.*

Acknowledgement

At first I would like to thank my supervisor Doc. RNDr. Milan Hrabovsky, CSc., for giving me the opportunity to study this important and useful subject and for his scientific support without which the finishing of the thesis would have been impossible. Further I would like to thank my father and my mother for their unexpendable, important and unique support. Special thank goes to my colleagues: J. Jenista, M. Konrad and O. Zivny for useful pieces of advice they gave me during preparing of computations and during writing of the thesis.

DECLARATION

I hereby declare that this thesis is based on the results found out by myself. Materials of work found out by other researchers are mentioned by references. I agree with lending of this thesis provided that it is done purely for noncommercial purposes and that the source is properly specified since several parts of this thesis are subjects to copyright.

_____

Signature of the author

Table of contents

Introduction

It is very common and useful to generate plasma in plasma torches not only in a field of scientific research but also in many industrial applications such as plasma spraying, cutting, processing of hard materials. Plasma torches as a sources of plasma jet have many advantages in comparison to other types of torches because plasma torches reach for example higher temperatures and higher velocities of working medium. One of possible and reasonable divisions of plasma torches is a division into: gas stabilized torches, water stabilized torches and hybrid water-gas stabilized torches. This division is based on type of medium that stabilizes the electric arc and isolates the arc from torch wall what prevents torch from heat damage. Such medium is inherently also used for generation of the plasma jet. An attachment of plasma torch to some reactor extends the usage of plasma torches to waste treatment or gasification of biomass. With respect to the fact that nowadays a majority of waste is still transported to and stored at dumps it is absolutely clear that big industrial plasma torches and plasma reactors will have large utilization in future since other possibilities of how to get rid of such dumps are difficult to reach. Hence, plasma arc waste processing represents an alternative to need for landfill. Such waste processing which uses extremely high temperatures produced by plasma arc destroy organic waste and produces flammable gas as a final product and also some amount of inorganic unburned fraction. Flammable gas can be subsequently used in chemical industry as a reactant or it can be used in power plants for production of electricity, representing a possibility how to store electrical energy in the form of chemical bonds. Gasification of biomass with consecutive burning of created gas in power plants is considered to be a net source of electricity. The energy efficiency of such gasification is about 60% what is not ideal but chemical species created in the process can be stored without any further energy losses what cannot be achieved in case of classic electrical energy storage (e.g. accumulators). The unburned fraction can be used for example as a construction material after some further processing. It is understandable that such waste processing cannot be applied to any radioactive substances (e.g. uranium) or toxic (e.g. mercury) or poisonous (e.g. lead) chemical elements since thermal plasma does not allow nuclear reactions to be realized but let us say toxic organic waste is eligible. For example 50 MW plasma gasification facility is planned to be built in Tees Valley (near Billingham), UK. In the facility it is planned to process about 350 000 tonnes of non-recyclable waste from near landfill per year. The facility is planned to enter full commercial operation in 2014 and in longer term it should possess a potential to produce hydrogen for commercial use, for example for public transport. This facility will become the largest of its kind all over the world. Some similar but smaller plants are already in operation in Japan, Europe and USA.

Nowadays there have also been developed several conventional methods of biomass gasification but plasma pyrolysis poses an advanced alternative to such conventional methods because it offers better control of temperature of the process, higher process rates, smaller volumes of reactors and better composition of final gas mixture. Plasma does not simply carry only the energy needed for the process but it additionally increases chemical reactivity of environment in the reactor because of presence of ions and excited species. Also plasma possesses higher enthalpy in comparison to gases used in conventional methods of gasification what means that energy needed for the process can be delivered by less amount of plasma and so chemical composition of final product will be less influenced by the plasma itself. An other important advantage of plasma waste disposal or plasma biomass gasification

to present high-end non-plasma industrial incinerators is that an amount of toxic compounds in the final gas product (e.g. dioxins) is more then ten times lower. This requires much less effort for cleaning of the final gas.

This doctoral thesis is dedicated to the last of the mentioned usages of plasma torches – gasification of biomass. More specifically it is devoted to numerical modelling of physical and chemical processes that occur in thermal plasma reactor during gasification of biomass. Numerical modelling of such processes is very important because it helps to understand the processes in the reactor and it enable us to enhance future experiments in corresponding way. The modelling gives us distributions of many physical properties of plasma and gas mixture in the reactor. Although these distributions are not exact, modelling has its important meaning because modelling is a much cheaper way how to obtain a knowledge of processes in the reactor or torch in comparison to experimental measurements. Such distributions cannot be easily measured directly either because of the presence of extreme physical conditions in the plasma jet area (area near the plasma torch) or because of complex geometry of the reactor. This is why processes in such reactors are still not fully understood.

The aim of the thesis is to create a parametric study of biomass gasification based on various diameters of wooden particles and to determine an approximate interval of wooden particle diameters that is suitable for use in specific thermal plasma reactor used in Thermal Plasma Department in Institute of Plasma Physics AS CR (hereafter only IPP CAS CR). Second aim of the thesis is to incorporate a description of turbulence into the numerical model of gasification of biomass. Effects of turbulence will be incorporated in two separate and independent ways. First will be valid for description of turbulence of physical flow of gases and their corresponding mixtures via standard k-ε model. Second way will be an implementation of turbulence and its effects on chemical reactions. All numerical computations will be carried out by Ansys Fluent® code. Plasma used in all experiments connected to gasification of biomass and also corresponding modelling of such plasma is in this thesis always considered to fulfil condition of LTE. In all computations presented in the thesis only wood (sawdust) is used for the gasification. Standard k-ε model was used as a turbulence model for all simulations since in [1] it was verified that all turbulence models available in Ansys Fluent® code give nearly the same results in our class of problems. And so usage of just one turbulence model is enough. Standard k-ε model is a little less computationally expensive in comparison to other available turbulence models and so the choice fell to this model since it was necessary to lower computational demand of the simulations as much as possible. However the usage of turbulence model is suitable because purely laminar model of flow gives results with differences visible enough as it is shown in [1].

The process of gasification of biomass in thermal plasma reactor powered by hybrid water argon plasma torch used in IPP CAS CR has never been numerically modeled with special emphasis on chemical reactions. In the past a similar model was developed by Stefaan Janssens in [6] where a study in Fluent® code was created for several different geometries of the reactor but chemical reactions of syngas production were not modeled there. Plasma and syngas were just modeled in [6] by respectively a fixed mixtures of H_2O-Ar and H_2-CO. On the other hand rich experimental investigations have been carried out in order to determine mole fractions of syngas and other chemical species at the exit tube of the reactor. Such experiments and corresponding results were for instance published in [7,8]. Numerical modeling of the internal part of torch itself and of the area near anode was also

extensively carried out because knowledge of torch properties and its capabilities is crucial not only in experiments of gasification but also for plasma spraying, plasma powder coating and so on. Methodology of modeling of the inside of this torch and resulting distributions of physical properties are for example given in [9,10]. Properties of plasma flow in the reactor are not just given by conditions and setting in the internal part of the plasma torch itself but also by a phenomena occurring near anode usually referred to as anode arc attachment. This is the reason why to study the physics of anode attachment. Physics of the attachment has not still been fully understood and a state-of-the-art of the attachment phenomena is given in [11,12].

The gasification of biomass has also other possible application in industry. As it has been mentioned above the process of gasification transforms electrical energy (represented by plasma arc) into chemical bonds energy of final gas mixture. Such gas mixture can contain higher energy content than primary biomass. Hence, gasification of biomass (intrinsically automatically combined with electrical energy storage) offers an alternative to fossil fuels. Gasification of biomass (coal, wood) also grants better manipulativeness of final syngas to primary biomass. Trasportation of syngas can be achieved for example by a system of pipelines while for solid biomass this is not an option. Most of the experiments with plasma pyrolysis have been performed with arc plasma torches with relatively high flow rates of plasma gas. Production of syngas from wood in plasma generated in ac air plasma torches is discussed in [13]. Coal gasification in hydrogen, air and steam plasma was studied in [14,15]. In [16] wood was gasified in steam plasma. The high flow rate of plasma provides good mixing of plasma with treated material but produced syngas contains components of plasma gas. For example nitrogen contained in air in the air plasma gasification can be used only as a energy carrier and also as a medium for chemical reactivity increase of the reactor environment since nitrogen is excited and partially ionized as well but at the end of the process nitrogen only drains thermal energy of the system. Such energy drain can be subsequently used only in some recuperation heat system And so the usage of mixtures of inert gas with hydrogen was used in [17] to eliminate this disadvantage but it increased the cost of the technology. Therefore steam was used as plasma gas in [14, 16].

Experimental setup of gasification process

The experimental setup of the reactor and all ancillary devices consist of 7 units as it is given in figure 1. The main idea of the experiment is that biomass is prepared and stored in raw material bin (unit 1), from where it is transported at corresponding feed rate by screw feeder (unit 2) directly into a reactor chamber (unit 3). Unit 1 and 2 represent hermetically closed system within which the pressure is automatically adjusted in order to ensure higher pressure than the pressure in the reactor to avoid leakages of gasses out of the reactor. Capacity of raw material bin is 30 kg of common biomass. Black dots in Fig.1 in the reactor chamber represents biomass itself falling freely downwards to the bottom of the reactor indicating the direction of gravitational force. Plasma torch (unit 4) is attached to the top of the reactor and it produces plasma flow (red belt) used for heating, mixing, depolymerization, gasification and ionization of biomass. In the reactor chamber the biomass is also a subject of complex chemical reactions that are not easy to describe. Processed biomass encounters plasma flow approximately 0.3 m below of the plasma entrance. Presence of plasma jet in the reactor makes all chemical and physical processes fast and also the environment in the reactor is chemically highly reactive. This high level of chemical reactivity is caused by presence of ions, excited species and radiation – mainly UV radiation of plasma jet. So called syngas is produced as a main result of all physical and chemical processes of gasification of biomass in the reactor. Syngas is a technical name for synthetic gas that consists of carbon monoxide and hydrogen. Slag basin (unit 5) is used for slag that can be eventually produced during the experiment especially in case of high feeding rate of biomass. Water cooling chamber (unit 6) is attached to the exhaust pipe of the reactor. This thermal plasma reactor is able to process maximally 60 kg/h of biomass and its nominal internal temperature of processed material is 1700 ^{o}C. The temperature in the reactor is not uniform and value of 1700 ^{o}C just represents an average value. Reactor produces a mixture of gases that are still too hot for some type of analysis. This is the reason why this mixture is cooled down in water cooling chamber prior to further gas analysis. The mass flow rate of water is automatically controlled to maintain the temperature of exhausted gas mixture at a level of 300 ^{o}C. In order to be able to exhaust final gas mixture into environment it is necessary to burn the final mixture because it contains dangerous or poisonous chemical species (such as carbon monoxide). This is done in combustion burner (unit 7). Eventually it is also possible to burn such gas mixture in combustion engine in order to produce some electricity but this possibility has not been used so far in IPP CAS. In industrial and commercial applications the energy produced by reactors of this type will be fully recuperated.

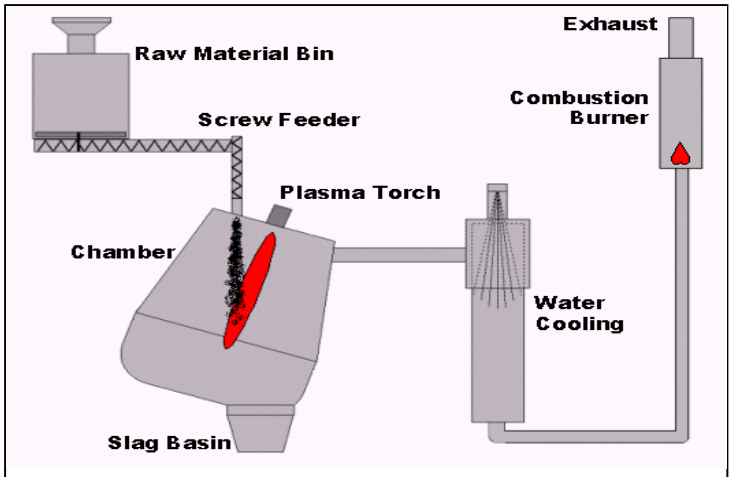

Fig. 1 Experimental setup of the thermal plasma reactor and corresponding auxiliary devices

This setup is only experimental and thus still not suitable for commercial usage.

Plasma reactor

The internal volume of the reactor chamber is 0.206 m^3. The reactor is constructed to operate at inner wall side temperature of 1100 ^oC– 1400 ^oC. Due to high average temperature of inner side of reactor walls it was necessary to reduce power losses to the walls as much as possible. That is why reactor walls are made of several layers of special refractory ceramic and other insulating materials of various thermal conductivities and of various resistances to high temperatures. It was absolutely

Fig. 2 2D-Cut of the computational grid-global view
Displayed plane: xy (z=0)

Fig. 3 2D-Cut of the computational grid-Anode area
Displayed plane: xy (z=0)

necessary to combine several insulating material together because refractory ceramic is able to withstand sufficiently high temperatures but its thermal conductivity is still very high according to our demands. And on the other hand the other insulating materials have low thermal conductivity but they cannot withstand high temperature without thermal degradation of themselves. Only a multi-level combination of such insulating materials can possess both wanted properties at once: low thermal con-ductivity and high thermal resistance. Width of thermal insulation of the reactor is 400 mm. Presence of such ceramic requires slow preheating of the reactor prior to experiment of gasification itself. Average preheating time of the reactor takes about 16 hours. Preheating is done by electric spiral unit with power input of about 20 kW. Fast temperature change could damage the ceramic insulation and so maximum allowed heating speed is 60 $^oC/h$. Outer side of reactor walls are cooled down by slow flow of cold water. Figs.2-3 show authentic views of the reactor during an experiment. Red colour in one of the reactor windows in Fig.3 indicates level of temperature inside the reactor and fast shutter CCD camera is visible to be attached to other window of the reactor. The CCD camera is used for spectroscopic measurements of thermal radiation from inside of the reactor.

In Fig. 2 there is a rotated view of the reactor and a column where several gas diagnostics and analysis is carried out prior to cooling down in water cooling chamber. According to caloric measurements of the water used for cooling the reactor it was determined that heat losses to the walls equal 22 kW.

Detailed scheme of the reactor is given in Fig. 4. Dark grey colour represents ceramic lining and light grey colour stands for the other insulating materials. Thermometers used for measuring the temperature of the walls are located at the inner border of the ceramic lining. As it was mentioned above the width of thermal insulation of the reactor is 0.4 m but this is exact only for reactor walls. Top of the reactor has narrower (worse) insulation and so thermal losses to the top of reactor are higher than they are to other reactor walls as it follows from experiment and also from numerical simulations. There are three places in the upper part of the reactor (not visible in Fig.4) where next inputs for additional gases are located. Input of such gases helps to control the composition of gas mixture in the reactor. The location of exhaust reactor tube (marked by green arrow in Fig.4) is again in the upper part of the reactor. Such location was selected in order to force produced gases to pass through the high temperature zone that is close to or directly at the plasma jet what additionally reduces an amount of unwanted chemical species (like dioxins) present in final gas. The reactor chamber is rotated in such a way that if we exclude the effect of plasma torch the gasified biomass can freely fall down through the centre of the reactor into slug basin. This rotation was applied in order to keep the biomass far away from reactor walls as long as possible and in order to reach plasma flow as soon as possible. Certain part of the biomass is gasified within its falling from waste input tube due to plasma jet. The rest (non-gasified part) reaches the bottom of the reactor where it is subsequently gasified due to the presence of hot gas flow. During the process of gasification the slug basin is separated from the reactor chamber in order to keep biomass in the reactor. The amount and behaviour of non-gasified part will be discussed later (in chapter: Results of the simulations and discussion) in detail. Setup of the gasification process and also of the reactor geometry (especially the top of the reactor) is a subject to changes according to up to date level of knowledge.

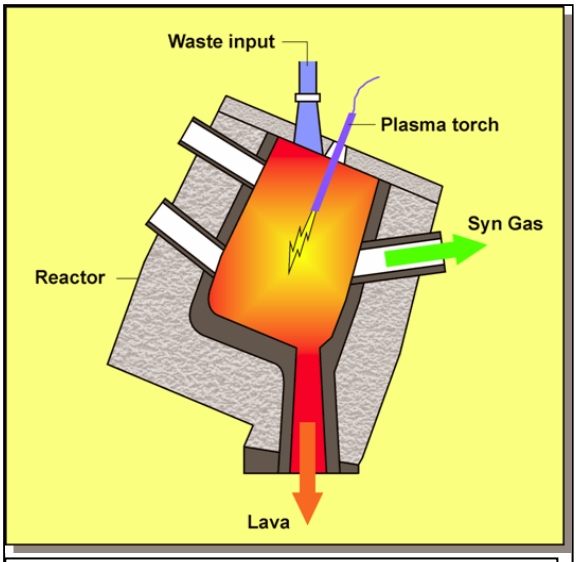

Fig. 4 Detailed scheme of the thermal plasma reactor

Plasma torches

Plasma torch is a device designed for plasma jet generation. A lot of various plasma torches have been developed and they are mainly categorized according to a way how the electric arc is stabilized. Stabilization of the arc means a mechanism that keeps the arc in desired and stable position. According to this division we recognize torches with: free burning arcs, wall stabilization, conventional vertex stabilization and magnetic stabilization. An other division of plasma torches can be based on type of electric current used for arc generation. It means division into AC and DC torches. AC plasma torches can be subsequently divided into single-phase or three-phase torches what simultaneously denotes a number of electrodes in such torches.

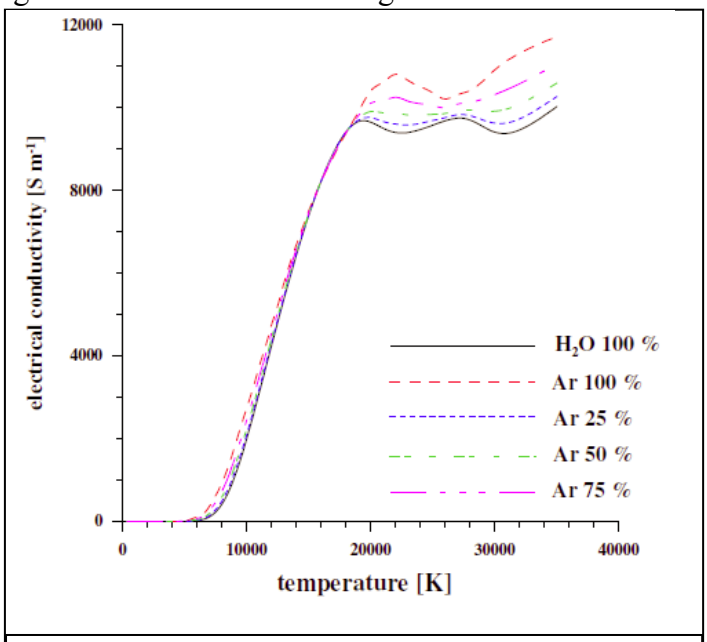

Fig. 5 Function of the electrical conductivity in terms of temperature for pure steam plasma (and also for several mixtures of steam plasma with argon)

Electric arc is always unstable. However usage of the arc in any plasma torch requires the arc to stay in its certain stable position. Whatever deflection of the plasma arc causes an interaction of the arc with some of the stabilization mechanism mentioned above and due to this interaction the arc is forced to return to its stable position. Local decrement of the arc temperature due to a contact of the arc with the cold wall, cold gas or cold liquid is the physical mechanism that causes a corresponding decrement of the electrical conductivity of the arc at the place of contact. With respect to the fact that the arc current is kept constant (usually by a source of current) an other area in bigger distance from the wall is nearly immediately heated up and hence the current (the arc) is deflected backwards. Function of the electrical conductivity in terms of temperature for pure steam plasma (and also for several mixtures of steam plasma with argon) is given in Fig. 5 where strong dependence of conductivity on temperature is obviously visible at scale from 1000 K to 20000 K. Such temperature scale is common for plasma arc torches. Further only hybrid water-gas stabilized torch will be described since such torch is used in our experiment and also in corresponding numerical simulations. This torch combines principles of stabilization used in gas and also in water torches. This torch was designed in the IPP CAS in Prague and it is protected by

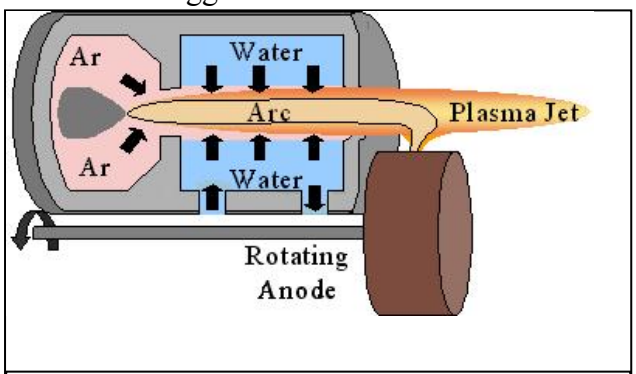

Fig. 6 Scheme of the hybrid water-argon stabilized plasma torch

copyright. The arc in this torch passes through two areas. In the first area it is stabilized purely by gas (in our case by argon) and in the second area the arc is stabilized by water (water vortex). Final plasma is thus composed of water-argon mixture. In this type of torch the physical properties (e.g. enthalpy, mass flow rate, velocity,) of the plasma jet can be changed in much bigger range than it is possible in torches with gas or liquid type of stabilization. The main advantage of an addition of argon to the stabilization mechanism is that it enables to control velocity and momentum of plasma. Plasma temperature is controlled here by the arc current and argon enables to control velocity and momentum of plasma independently of the plasma temperature. The scheme of the hybrid plasma torch is given in Fig. 6. The arc begins at cathode (the grey part that is surrounded by argon) which is cooled by flowing argon. Then argon plasma arc enters second part of the torch which is cooled by tangential supply of water. Arc ends at anode that rotates at speed of about 2800 RMP. Rotation of anode is required because it helps significantly to lower an intense thermal destruction of the anode caused by an attachment of the arc but still the anode is slowly being damaged during the operation of the torch. In order to lower hereafter the thermal damage of the anode a water cooling of anode was used and the anode is thus made of copper. It is interesting to mention that although anode is made of copper and it slowly vanishes during the experiment

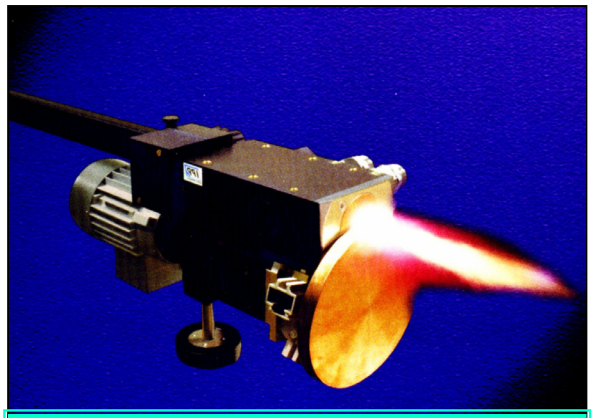

Fig. 7 Photograph and a basic operational parameters of the hybrid water-gas plasma torch

Table 1

Comparison of the enthalpy and temperature of various torches for waste treatment

Laboratory	**Type**	**Power (kW)**	**Plasma Type**	**Mean Enthalpy (MJ/kg)**	**Temperature (K)**
IPP CAS	WSHP-500	150	Water argon	225	15000
IT RAS Novosibirsk	EDP 217	150	steam	30	3600
IT RAS Novosibirsk	EDP 148	60	steam	60	4500
Westinghouse	MARC3	300	nitrogen	7	5000
IPE RAS St. Petersburg	EAG 6	250	nitrogen	16.7	3600
Kobe Steel, Ltd.		300	nitrogen	17-34	6300-7500

the element copper has never been detected by the CCD camera via spectroscopic measurements of thermal radiation coming out from the reactor. Probably the amount of copper is below the detection limit. Rotation of anode is provided by synchronous electric

engine. A photograph and a basic operational parameters of the hybrid water-gas plasma torch is given in Fig. 7. In case of this torch the plasma has very high enthalpy (about 200 MJ/kg), very high mean temperature (about 15000 K), very high velocity and so high turbulence as well. This plasma torch can operate at arc current from 300 A to 600 A and so other physical properties varies also within corresponding intervals as it is given in Fig. 7. The diameter of anode is about 20 cm and so it is possible to make an imagination of size and dimensions of the torch according to Fig. 7. Numerical simulations in this thesis were carried out for arc current of 400 A (most typical case) and for such current all other plasma torch parameters are listed in Table 3. Basic comparison of physical properties of this hybrid plasma torch and some other plasma torches used at other laboratories all over the world is listed in Table 1. With power input of 150 kW what is relatively just an average value among power inputs of other torches compared in the table the mean plasma temperature of 15000 K clearly shows the superiority of hybrid gas-water torch used in IPP CAS.

Computing procedure

For standard k-ε model used for description of turbulence following assumptions were applied: the plasma flow is turbulent and subsonic. Radiation effects and magnetic field are neglected and gravitational force is included in computations. Steam plasma is considered to be in local thermodynamic equilibrium. No user defined sources were implemented to governing equations. The inner total volume and dimensions of calculation domain (i.e. reactor chamber) that is presented in Figs. 2-4 is given in Table 2. All numerical simulations presented in the thesis are carried out corresponding to real dimensions at scale ratio1:1. Dimensions of the domain embrace not only the reactor chamber itself but also the exhaust pipe and all parts necessary for fixing of the plasma torch to the reactor chamber. As the real flow in the reactor is only mildly compressible we decided to neglect the compressibility effects on the flow and to use incompressible approach and pressure based solver with absolute velocity formulation in all the calculations. This pressure based solver is based on Navier-Stokes solution algorithm. SIMPLE scheme was used for pressure-velocity coupling. Green-Gauss cell based gradient evaluation method was used for computations of gradients of any scalar φ at the corresponding cell centre. Physical properties of nitrogen, hydrogen, carbon monoxide and steam plasma used in the computations, namely: density, heat capacity, thermal conductivity and viscosity were computed assuming existence of LTE by methods described in [25,26]. These properties were defined in all calculations in piece-

Table 2

Internal volume	0.206 m^3
Height (y-coordinate)	1.102 m
Width (x-coordinate)	0.793 m
Depth (z-coordinate)	0.57 m

Table 3

Mean velocity	v=2635 m/s
Centerline velocity	v_c=4407 m/s
Mean temperature	T=14500 K
Centerline temperature	T_c=23000 K
Mean enthalpy	H=185 MJ/kg
Mean density	$\rho=3.64x10^{-3}$ kg/m^3
Centerline density	$\rho_c=1.23x10^{-3}$ kg/m^3
Reynolds number	Re = 786
Mach number	M=0.445
Power input	P=106.8 kW
Arc current	I=400 A
Mass flow rate	Q_m=0.272 g/s

wise linear form and they are only temperature dependent as we employ incompressible flow. These properties embrace effects of high temperatures (up to 20000 K) namely dissociation of molecules and subsequent corresponding (also multiple) ionization of atoms. At a time of my numerical simulations of gasification, physical properties of carbon dioxide were not available at the level provided by methods described in [25,26] and so temperature dependence of density of CO_2 was just calculated by use of the equation of state of ideal gas for temperature range from 300 K to 2000 K and it is implemented in further computations again in piece-wise linear form containing 16 intervals. Upper temperature limit of 2000 K was applied according to an assumption that CO_2 as a oxidizing agent is present mainly in low temperature areas of the reactor and that fraction of CO_2 in high temperature areas (arc area) is extremely low.

Plasma jet characteristics at the input of the reactor correspond to the experimental conditions as given in [23, 24] and are given in Table 3. These plasma jet characteristics are used as inputs for the numerical computations. Grid used in all our simulations contained approximately 1.2 million nodes and was of variable node density. It means that close to plasma jet input (where velocity of steam plasma approaches the value of 2635 m/s) the node density is ten times higher than it is in areas of low velocity magnitudes (e.g. in lower parts of the reactor chamber and in exhaust pipe). In other words the density of the grid is higher in areas where large gradients are expected. Grid was purely tetrahedral because in majority of computational domain it was not possible to determine in advance the prevailing direction of flow. Graphical representation of tetrahedral cell is given in Fig. 8. Advance determination of flow direction was possible only in small area representing a part of internal volume of the torch itself and hence in such area the hexahedral uniform grid was used. Third-order MUSCL scheme was applied to the grid to reduce numerical diffusion and due to the use of this scheme the computation possesses third-order accuracy for diffusive and conductive terms. All simulations were solved with single precision because it was sufficient according to our previous experiences. Average net time of one computation was 4 days. All computations were performed on PC with characteristics given in Table 4.

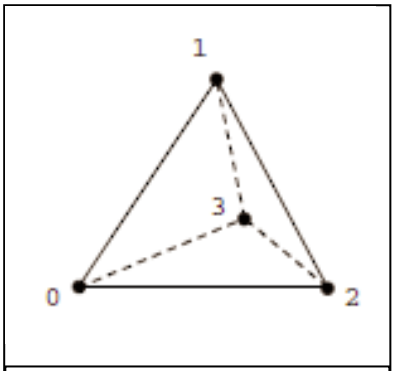

Fig. 8 Graphical representation of the tetrahedral cell

All boundary conditions of the computational domain are set according to known experimental values since major purpose of this modelling is to find out distributions of physical properties in internal parts of the reactor. Heat losses to the reactor walls were always modelled by prescribed heat flux and only in one special case the wall temperature of the reactor was constantly set to 1300 K because such wall temperature was obtained at the experiment. This heat flux was not constant but was computed via conduction of heat in solid reactor walls with certain width of walls and with subsequent convection of heat via cooling liquid that is present at outer side of reactor walls. The temperature of this cooling liquid (water) is prescribed and constant. This heat flux to the walls was described by constant heat transfer coefficient that was the same for all parts of reactor chamber representing cumulative thermal insulation ability of all ceramic and other insulation layers For reactor chamber and connected pipes the value of 5 $wm^{-2}K^{-1}$ was used. For purely metallic insulating parts the

value of 10 $wm^{-2}K^{-1}$ was used and for anode that is made of copper the value of 50 $wm^{-2}K^{-1}$ was used. Width of reactor walls for the need of

Table 4	
Number of processors (Intel Xeon E5-2670)	2
Number of physical cores	16
Number of threads	16
Available RAM	16 GB
Used CFD software	Ansys Fluent®, version: 14.5
Operating system	Windows 7 Professional, 64bit
Computational speed-according to Cinebench®	18.8

computation of heat losses were 0.4 m for reactor chamber and 0.1 m for pipes. Width of anode wall was 5 mm and width of walls made of purely metallic parts was 20 mm. Temperature of cooling liquid was constantly set to 300 K. All these setting was made in order to achieve thermal losses of 22 kW to the reactor walls (including pipes) and separately of 8 kW to the anode.

The discrete phase (i.e. wooden particles) in Fluent code is modelled via Euler-Lagrangian discrete phase model (that follows Euler-Lagrange approach). This means that the fluid phase (gases + liquids) is treated as a viscous continuum and discrete phase is computed by tracking of corresponding number of single solid particles. This approach is based on assumption that solid particles do not interact among each other at all. This is why the volume occupied by solid particles must be lower than volume occupied by viscous continuum otherwise this approach is not applicable. Discrete phase (that is dispersed into the viscous continuum) can exchange mass, momentum and energy with the continuum. In all of the simulations here in the thesis the discrete phase does not interact chemically with fluid phase. All chemical reactions here are defined only as a "fluid-fluid" type. The wooden particle trajectories are computed individually every 5^{th} iteration of the fluid phase. With respect to the fact that solid particles (due to their high density in comparison to density of fluid phase) do not react quickly to changes of motion of surrounding fluid phase it is suitable to calculate the particles trajectories not every fluid iteration. This saves computational time significantly.

Steam plasma used in this computation is not pure water but it is a mixture of 95% of water and of 5% of argon. Physical properties of this specific steam-argon plasma (mentioned so far just as a steam plasma) were computed by methods described in [25,26] with respect to 5% argon content.

Physical properties of all fluid species present in the reactor (i.e. steam plasma, CO_2, H_2O, N_2, CO and wood volatiles) as described above are computed separately and they are valid for pure species (except for steam plasma that has been calculated from the beginning as a mixture of steam and argon). For the need of computation it is necessary to know physical properties of corresponding mixture of all present species for various molar fractions of the species and for all temperature range of the experiment. However it is not possible here to generate tables of all values for temperature step little enough to fit our computational needs and so adequate mixing laws of species must be defined in Fluent code that would alternate such tables. In this manner for mixture density determination the volume-weighted mixing law is used defined by following equation:

$$\rho = 1 / \sum_{i=1}^{N} \frac{Y_i}{\rho_i} \qquad \text{(eq.1)}$$

where Y_i is mass fraction of species i and ρ_i is density of species i. N is total number of species in the system. Specific heat of mixture is determined by following mixing law:

$$c_p = \sum_{i=1}^{N} Y_i c_{p,i} \qquad \text{(eq.2)}$$

where Y_i is the same as in eq.9, and $c_{p,i}$ is specific heat capacity at constant pressure p for species i. Thermal conductivity of the mixture is determined by following equation:

$$k = \sum_{i=1}^{N} Y_i k_i \qquad \text{(eq.3)}$$

where Y_i is the same as in eq.9, and k_i is thermal conductivity of species i. Since we do not use ideal gases in our Fluent computations it is not possible to use more exact formula available in Fluent that is based on kinetic theory. For the case of mixing of non-ideal gases we have to restrict ourselves to computation of the mixture thermal conductivity on a simple mass fraction average of the pure species as it is given by eq.9. And finally for viscosity of the mixture following rule is applied:

$$\mu = \sum_{i=1}^{N} Y_i \mu_i \qquad \text{(eq.4)}$$

where μ_i is viscosity of species i. Again it is not possible to use formula available in Fluent derived form kinetic theory as we do not mix ideal gases.

In Fig. 9 the scheme of wooden particle interaction with plasma flow is given. Wooden particle enters region with temperature higher than the volatilization temperature as

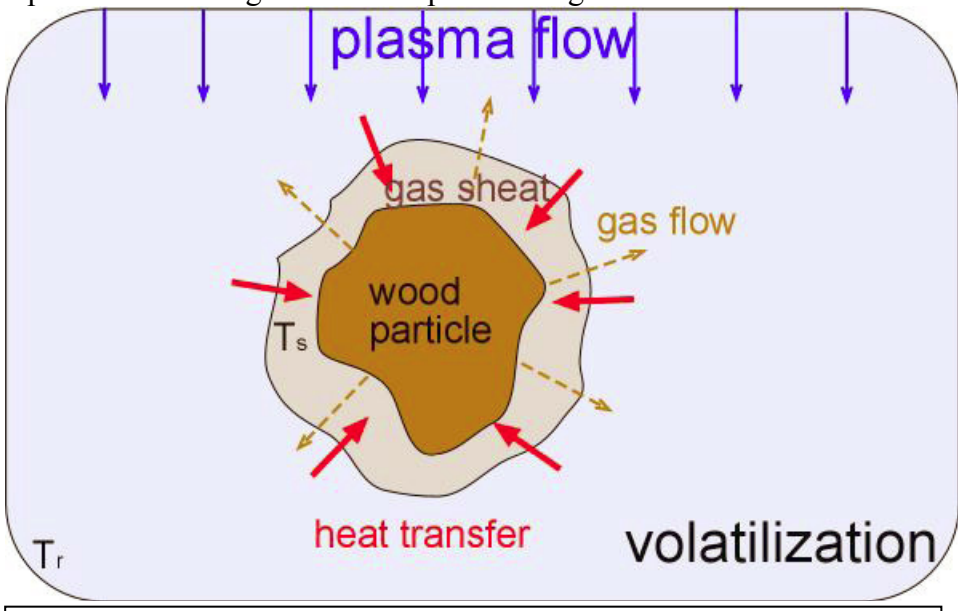

Fig. 9 Scheme of wooden particle interaction with plasma flow

it is given in Table 6. Due to temperature high enough a heat transfer from plasma towards wooden particle is established. In Fig 9 this heat transfer is marked by red arrows. This transfer continuously volatilizes (or boils if boiling temperature is reached as defined in Table 6) the particle and as a result of such volatilization and boiling a creation of a thin gas layer of "wood volatiles" species is present around the particle. This layer is represented in Fig 9 by light grey colour (gas sheath). This layer is already a subject to all chemical reactions defined in the computations and also a subject to laminar or turbulent mixing with surrounding flow. Wooden particle represents a significant source of gas phase since during volatilization and boiling of each particle the cold solid wood is being transformed into hot gas what brings volume change of the order of 10^3.On the other hand this layer possess automatically some thermal insulation for wooden particle what is undesired but inevitable because "wood volatiles" species (insulating particle gas layer) has low thermal conductivity as it is common for majority of gases. This is why solid particles can pass through high temperature regions of the reactor without complete volatilization. The ability of solid particle to withstand plasma flow strongly depends on the diameter of the particle. The aim of the thesis is to determine this dependence. Important effect acting to the solid particle is the drag force. This force denotes together with gravitational force the trajectory of the particle. This force is defined in governing equations chapter in (eqs. 20, 21). Thermophoretic force is important especially for small particles. Such particles released into a gas phase with temperature gradient are subjects to a force acting in the opposite direction to that gradient. Thermophoretic force is the last force that was employed for particle trajectory determination and it is also defined in governing equations chapter in (eq. 30). Other forces available in Fluent code acting on particles were not modelled due to low importance for our class of problems (like Brownian force since we do not model sub-micron particles) and also due to the fact that an incorporation of other forces would have increased the computational demand.

Computational grid used in numerical simulations of biomass gasification is of the highest node density ever used for plasma gas reactor used in IPP CAS. 2D cut of this grid is

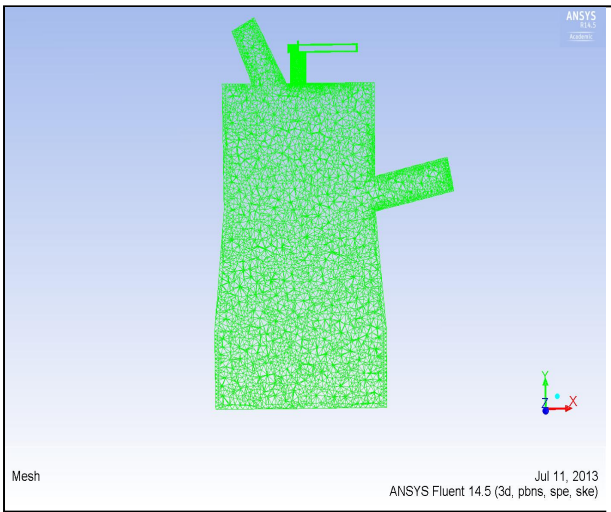

Fig. 10 2D-Cut of the computational grid-global view
Displayed plane: xy (z=0)

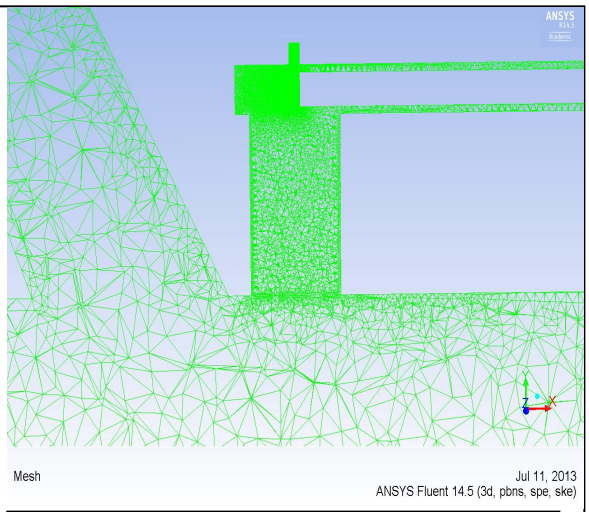

Fig. 11 2D-Cut of the computational grid-Anode area
Displayed plane: xy (z=0)

presented in Fig. 10 where global view is given. Although node density is not constant from global point of view the node density within the reactor chamber itself is nearly constant

because physical condition in the reactor chamber are not extremely spatially different. The situation at the arc area and at some parts of the anode area is different and so the node density is much higher there as it is given in Fig. 11. There are two most visible interfaces where the density of computational grid is greatly changed: between arc area and plasma inlet pipe and between plasma inlet pipe and the reactor chamber as it is visible in Fig.11.

In Fig. 12 a 3D view of the geometry of the upper parts of the reactor and anode area is given. The grid itself is only displayed partially there because it is too dense for complete display and the part of the grid corresponding to the internal volume of the plasma torch is not

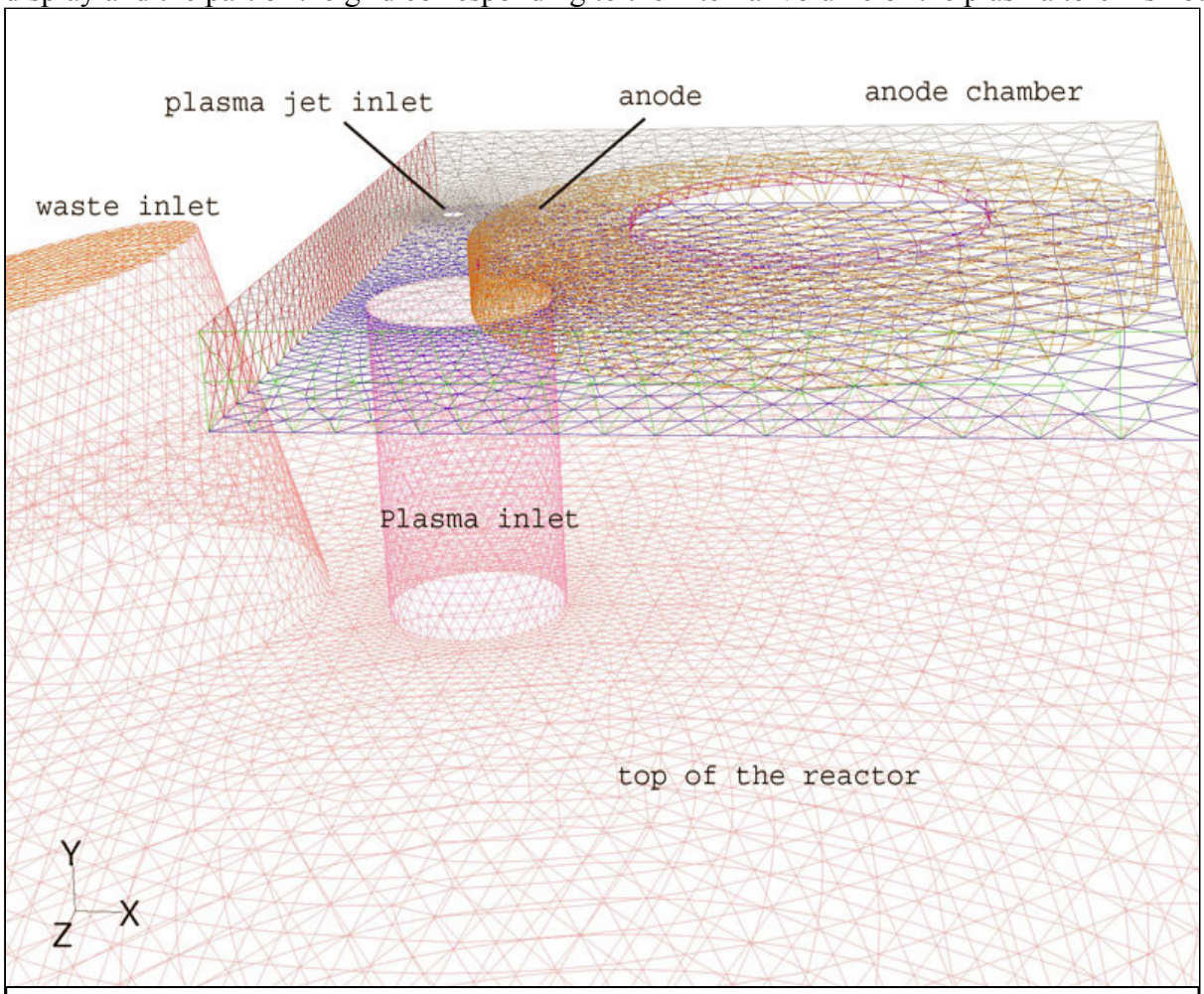

Fig. 12 Three dimensional view at the top of the reactor geometry and the anode area

displayed as it is not a subject of the thesis and presence of such volume in this computation serves only for creation of corresponding realistic profile of physical properties out of constant boundary condition for velocity and temperature.

As it has been mentioned above in this section pressure based algorithm is used for all computations. More specifically this algorithm is segregated and principal scheme of this algorithm is given in Fig. 13. U; V and W means velocities in corresponding coordinates x; y and z and they are computed separately according to a previously updated values of pressure and face mass fluxes. Generally speaking all governing equations in this algorithm are solved one after another what means that Physical and chemical properties are updated every iteration and at the very beginning of the computation the properties are set according to first

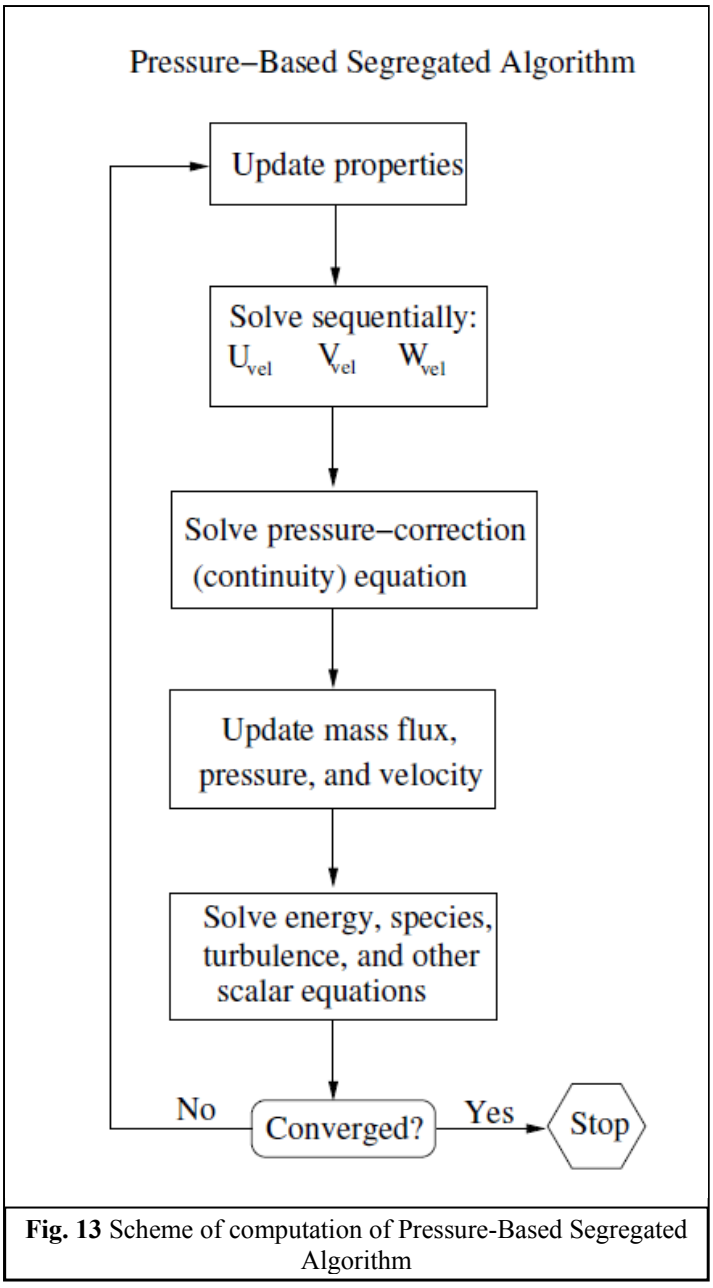

Fig. 13 Scheme of computation of Pressure-Based Segregated Algorithm

initialization that follows from boundary conditions set prior to the computation. The whole computational process is iterative with average number of approximately 30000 iterations per one computation until converged solution is reached. This number is higher than usual because some boundary conditions and also several other parameters (mainly mean diameter of wooden particles and mass flow of wooden particles) cannot be set at the beginning of the computation to values corresponding to experimental values because the computation would crash. After reaching of partially converged solution for intermediate values of boundary conditions and parameters it is possible again to more adjust these values towards desired boundary conditions. Equations listed in Fig. 13 are given in the governing equation chapter. Convergence criteria for all computations presented in the thesis are given in results of the simulations and discussion chapter. More details on this solver is given in [27].

Description of chemical processes of the gasification of wood

In several previous numerical simulations the process of syngas production was described by just one chemical reaction (reaction 2). This approach was not satisfactory because it required all three reactants to be present at least at some level at enough number of computational cell within computational domain. However this requirement cannot be generally fulfilled although the chemical reaction was balanced and so corresponding reaction yield was very low. This was the reason why an approach implementing two chemical reactions was used. Reaction 2 was kept further without any changes but reaction 1 has arisen:

$$C_{1.69}H_{2.37}O + 0.69\ CO_2 \longrightarrow 2.38\ CO + 1.185\ H_2 \qquad \text{(reaction 1)}$$

$$C_{1.69}H_{2.37}O + 0.121\ H_2O + 0.569\ CO_2 \longrightarrow 2.259\ CO + 1.306\ H_2 \qquad \text{(reaction 2)}$$

Reaction 1 says that wood can be transformed to syngas without chemical presence of steam plasma provided that temperature is high enough. Reaction 2 says that wood can by transformed to syngas not only by reducing of CO_2 but also by reducing of H_2O. H_2O in all reactions means steam plasma or more accurately it represents all the species that are created of steam by heating high enough but from global chemical point of view it is still water. Energy changes in all chemical reactions are defined purely by standard state enthalpies of particular species. Standard state enthalpies of all present species are listed in table 5. Enthalpy reference temperature for all species is T_{ref}= 298.15 K. Wood is represented in Table 6 and also in reactions [1,2] by formula $C_{1.69}H_{2.37}O$ what represent one "monomer" of cellulose or more precisely one "monomer" of wood used in our experiments. Formula $C_{1.69}H_{2.37}O$ was determined in our institute by corresponding elemental analysis of used wood sample. The principal idea of gasification and production of syngas in numerical simulations used in this thesis is as follows: wood in a form of wooden particles of various diameters is injected into the reactor as it is shown in fig.4. Such wooden particles are represented by material: wood-solid. Basic physical properties of such solid wood used in the computation are given in Table 6. After injection, wooden particles are heated up but they do not chemically react with any other species regardless of temperature. Wooden particles are inert "droplets" of solid wood that are subjects to heating, after appropriate (vaporization) temperature is reached they are also subjects to evaporating and after boiling point is reached they start to boil. All physical properties of solid wood given in Table 6 are constants. Density, specific heat, thermal conductivity of solid wood were taken from fluent database and also these properties are widely available in literature. Latent heat of solid wood was set to 0 because it is nearly impossible to define such value since wood has extremely complex mechanism of transformation from solid state to liquid (or gas) state. Such transformation embraces many

Table 5

Chem. formula	Standard State Enthalpy [J/kmol]
CO_2	-3.935324 e+08
$C_{1.69}H_{2.37}O$ (vap.)	-2.548 e+08
CO	-1.105396 e+08
H_2	0
H_2O	-2.418379 e+08
N_2	0

various chemical substances that also chemically react not only with many of them but also with an ambient oxidizer agent (e.g. air, if present of course) during heating and during depolymerization of solid wood. Vaporization temperature, boiling point and heat of pyrolysis were taken from [2] and being a positive number heat of pyrolysis represents a positive contribution to the energy balance. It means that pyrolysis is slightly exothermic process in this modelling. Value of 4170 J/kg is small and has rather a symbolic meaning in global energy balance. It is important to mention that such material properties like heat of pyrolysis are not easy to acquire because such values are relatively different in different papers and it is not absolutely clear which one is most suitable for our specific gasification experiment. Volatile component fraction at the level of 100% means that all solid wood is capable of volatilization and that no unburnt fraction (like char or ash) is formed. It was quite necessary to exclude unburnt fraction from calculation at least at first approaches to numerical modelling of gasification of wood because such unburnt particles were source of numerical diffusion of computational errors what caused computation to fail relatively often. Values denoting vaporization temperature and boiling point in Table 6 are reliable because they are widely used in modelling of gasification.

Table 6

Physical property of solid wood	Corresponding value
Density	700 kg/m^3
Specific Heat	2310 Jkg^{-1}K^{-1}
Thermal Conductivity	0.173 Wm^{-1}K^{-1}
Latent Heat	0 J/kg
Vaporization Temperature	513 K
Boiling Point	650 K
Volatile Component Fraction	100 %
Heat of Pyrolysis	4170 J/kg

Evaporating and boiling are the only two ways in this model how solid wood is transformed into volatilized wood. This volatilized wood is of gas state and its chemical formula is $C_{1.69}H_{2.37}O$. Volatilized wood is sometimes called wood volatiles and it is a subject to reaction 1 and to reaction 2. Basic physical properties of such wood volatiles are given in Table 7. Density of wood volatiles was computed by me with use of equation of state of ideal gas with respect to its molecular weight and this density was computed for standard conditions. Density of wood volatiles is constant regardless of temperature. This is strong assumption and also strong simplification of real state but this assumption is based on the fact that wood volatiles are chemically highly reactive at temperatures higher then 900 K and so presence of wood volatiles in the computational domain is expected to be very low. Also it is suitable to lower computational difficultness as much as possible since one computation takes long time. Values of specific heat, thermal

Table 7

Physical property of wood volatiles	Corresponding value
Density	1.5 kg/m^3
Specific Heat	1500 Jkg^{-1}K^{-1}
Thermal Conductivity	0.0454 Wm^{-1}K^{-1}
Viscosity	1.72 e-05 kgm^{-1}s^{-1}
Molecular Weight	38.65 g/mol

conductivity and viscosity of wood volatiles were taken from fluent material database and they are constants because of the same assumption that is valid for density. Standard state enthalpy of wood volatiles is given in Table 5.

For the need of flow governing equations (eqs. 13-16) a speed of chemical reactions is determined by a net source of chemical species i. This net source is denoted by symbol R_i . For laminar flows the net source of a chemical specie i due to chemical reactions is given as the sum of the Arrhenius reaction sources over the N_R reactions where specie i is present:

$$R_i = M_{w,i} \sum_{r=1}^{N_R} \hat{R}_{i,r} \qquad \text{(eq.5)}$$

where $M_{w,i}$ is the molecular weight of species i and $\hat{R}_{i,r}$ is the Arrhenius molar rate of creation of species i in reaction r. In our computations we made next two assumptions, namely that all chemical reactions taking place in the reactor ale only non-reversible and that the net effect of third-bodies on the reaction rate is zero. Hence the Arrhenius molar rate takes a simplified form:

$$\hat{R}_{i,r} = k_{f,r} \prod_{j=1}^{N} [C_{j,r}]^{(\nu'_{j,r} + \nu''_{j,r})} \qquad \text{(eq.6)}$$

where $k_{f,r}$ is forward rate constant for reaction r; $C_{j,r}$ is molar concentration of species j in reaction r; $\nu'_{j,r}$ is rate exponent for reactant species j in reaction r and $\nu''_{j,r}$ is rate exponent for product species j in reaction r.

The forward rate constant for reaction r, $k_{f,r}$, is computed using the well-known Arrhenius expression:

$$k_{f,r} = A_r T^{\beta_r} e^{-E_r / RT} \qquad \text{(eq.7)}$$

where A_r is the pre-exponential factor for reaction r; β_r is temperature exponent for reaction r; E_r is activation energy for the reaction r and R is the universal gas constant. In order to compute $\hat{R}_{i,r}$ in accordance with (eq.1-3), the values of corresponding parameters are given in Table 8. Temperature exponent β_r is set to 0 in all reactions. Rate exponents for all product species in all

Table 8

Parameter	Corresponding value
Rate exponent for wood volatiles in reaction 1	0.2
Rate exponent for CO_2 in reaction 1	1.3
Pre-exponential factor in reaction 1	1.3 e+10
Activation Energy in reaction 1	1.505 e+08 J/kmol
Rate exponent for wood volatiles in reaction 2	0.2
Rate exponent for H_2O in reaction 2	1.3
Rate exponent for CO_2 in reaction 2	1.3
Pre-exponential factor in reaction 2	1.3 e+10
Activation Energy in reaction 2	1.505e+08 J/kmol
Rate exponent for CO in all reactions	0
Rate exponent for H_2 in all reactions	0

reactions (it means for CO and H_2 are set to 0. Values for activation energies and pre-exponential factors for both chemical reactions were taken from [3]. Rate exponents for all species for all reactions were taken from Fluent database.

For turbulent flows, $R_{i,r}$ (that is subsequently used in (eq.1) instead of $\hat{R}_{i,r}$) is calculated by (eq.4) and (eq.5) as follows:

$$R_{i,r} = \nu'_{i,r} M_{w,i} A \rho \frac{\varepsilon}{k} \min_R \left(\frac{Y_R}{\nu'_{R,r} M_{w,R}} \right) \qquad \text{(eq.8)}$$

$$R_{i,r} = \nu'_{i,r} M_{w,i} AB \rho \frac{\varepsilon}{k} \frac{\sum_P Y_P}{\sum_j^N \nu''_{j,r} M_{w,j}} \qquad \text{(eq.9)}$$

where index i denotes species i; index r denotes reaction r; Y_P denotes the mass fraction of any product species P; Y_R denotes the mass fraction of particular reactant R; A =4; B=0.5. A and B are empirical constants.

And subsequently the smaller of this two values of $R_{i,r}$ (given by (eq.4) and (eq.5)) is used as a final $R_{i,r}$ in (eq.1). With respect to the fact that there are two competing ways (one way for laminar flow and one way for turbulent flow) how to evaluate the net source of chemical species i (denoted by symbol R_i), it is necessary to distinguish whether the flow is laminar or turbulent from point of view of chemical reactions. For this purpose a turbulence is present if a fraction $k/\varepsilon>0$. If $k/\varepsilon<0$ the flow is considered to be laminar. Quantities k and ε represent turbulence kinetic energy and its rate of dissipation respectively. Note that this criterion is applicable only for a choice of a way of computation of $R_{i,r}$. It is also suitable to mention here that for determination whether physical flow is laminar or turbulent the Reynolds number R_e is used. More details on turbulence chemistry interaction model is given in [4]. Physical properties of solid wood used in the gasification are given in Table 9. Solid wood (wooden particles) enter the reactor through waste input as it is shown in Fig.3. At that moment wooden particles have initial velocity (velocity magnitude) as it is given in Table 9 and since this moment their velocity is increased only by gravitational force or it is changed by surrounding flow field. Total flow rate (or total mass flow rate) of wooden particles as given in Table 9, is constant for all three investigated cases and it corresponds to flow rate of 25kg/h of wood with 7% moisture content what is one of a typical experimental case of gasification in our experiments. In order to simplify the computation within reasonable limitations of course the moisture content of wood was set to 0 and so the value of 23.5 kg/h was obtained. Such decrement of wood

Table 9

Variable	Corresponding value
Temperature	301 K
Velocity Magnitude	0.03 m/s
Total Flow Rate	0.00646 kg/s (=23.5 kg/h)
Min. Diameter	0.1 mm; 1 mm; 10 mm
Max. Diameter	0.3 mm; 3 mm; 30 mm
Mean Diameter	0.2 mm; 2 mm; 20 mm
Spread Parameter	3.5
Number of Diameters	10

moisture (oxidizing agent) led to required higher mass flow rate of CO_2 that enters the reactor via the same waste input as solid wood does. According to an amount of oxidizing agents in the gasification reactions the gasification of wood can be carried out in three different ways: 1. no oxidizing agent is added (in such case we speak of pyrolysis) and so syngas and a small amount of solid carbon is produced; 2. stoichiometric amount of O_2 is added and this time only syngas is produced; 3. stoichiometric amount of CO_2 is added and therefore again only syngas is produced. Gasification modelled in this thesis is of the third type and corresponding scheme of chemical equation is:

$$\text{wood} + (n_C - n_O)CO_2 \longrightarrow (2n_C - n_O)CO + n_{H2}H_2 \qquad \text{(eq.10)}$$

where $n_C = c/M_c$; $n_{H2} = h/2M_H$ and $n_O = o/M_o$ are the molar concentrations of carbon, hydrogen and oxygen in wood with the mass fraction of carbon, hydrogen and oxygen equal to C, H and O respectively. In order to fulfil the requirement of stoichiometric amount of CO_2 in (eq.6) the input mass flow rate of CO_2 was set to 134.85 slm (=4.0455 g/s of CO_2). In real experiment there are always more products than it is defined by (eq.6) but fraction of syngas (i.e. $CO+H_2$) is the highest of all as it is given in Fig.14. Parametric study of gasification of wood was carried out with respect to 3 different diameters of wooden particles with values given in Table 9. Diameters of particles were mainly equal to mean diameter and never exceeding their corresponding minimum or maximum diameter value. Diameters of particles were chosen in order to represent most common conditions of gasification in the reactor. Wooden particles of mean diameter = 0.2 mm represent wood dust, particles with mean diameter = 2mm represent sawdust and particles with mean diameter = 20mm represent just a size of a larger pellets of various types of available biomass (e.g. polyethylene pellets). Not all wooden particles used in the computation are of the same size. Within each of the three cases of the study the particle diameters follow Rosin-Rammler diameter distribution, which is given by (eq.7):

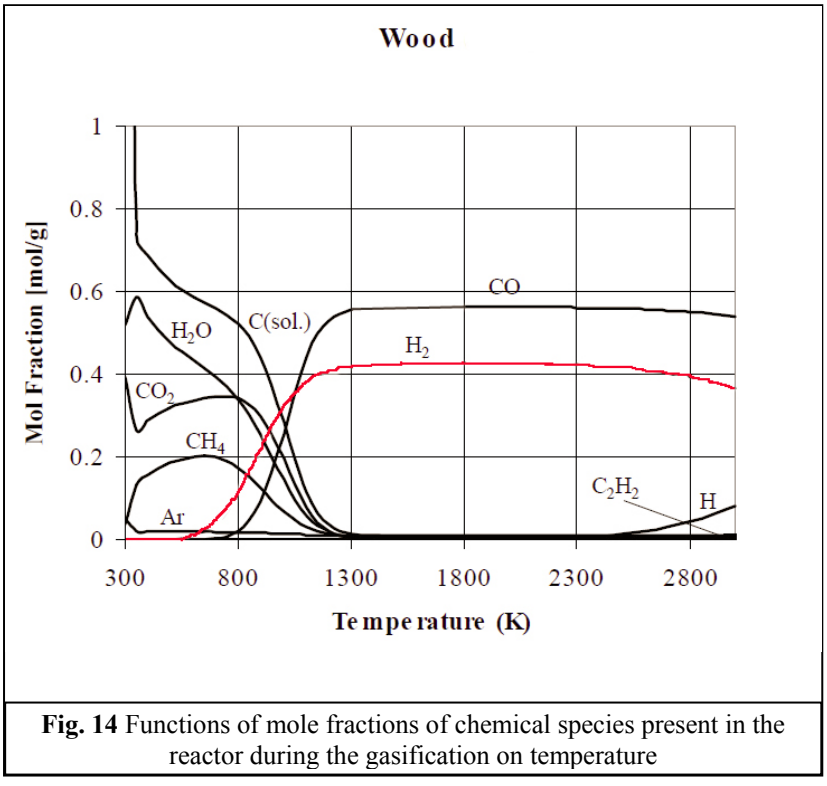

Fig. 14 Functions of mole fractions of chemical species present in the reactor during the gasification on temperature

$$Y_d = e^{-(d/\bar{d})^n} \qquad \text{(eq.11)}$$

where Y_d is the mass fraction of particles with diameter greater than d; d denotes the particle diameter; $\bar{d}$ denotes the size constant and n is the size distribution parameter. The spread parameter given in Table 9 is the exponential factor n in (eq.7).

Fig.14 gives us an information what is an approximate efficiency of gasification of wood in real experiments in our reactor in terms of temperature. Except syngas, also other chemical species are produced especially at higher temperatures (such as ethylene) but yield of such species is very low. The reason for production of such secondary chemical product is that real chemical equations describing the process of gasification are complex and that the number of such reactions is very large and thus it is impossible to embrace them all in any model. It is important to mention that according to Fig. 14 there is a temperature limit of about 1200 K that denotes the minimum temperature required for high quality syngas production. On the other hand in case of numerical modelling the situation is different because only species defined as a product species of particular chemical reactions can be formed. Other species present in the outflow pipe of the reactor are just reactants that due to not ideal mixing or low temperature were not able to give corresponding product species.

For the sake of completeness it is suitable to mention here that when we are solving a chemically reacting flow using the finite-rate or eddy dissipation model (what is just our case this time), we will need to define the standard state enthalpy (also known as the formation enthalpy or heat of formation), h^0_j for each species j. These inputs are used to define the mixture enthalpy as:

$$H = \sum_j m_j \left[h_j^0 + \int_{T_{ref,j}}^{T} c_{p,j} dT \right] \qquad \text{(eq.12)}$$

where $T_{ref,j}$ is the reference temperature at which h^0_j is defined, $c_{p,j}$ is specific heat capacity at constant pressure p for species j. Standard state enthalpies, for the purpose of this thesis and corresponding numerical simulations are input in units of J/kmol (as it is given in Table 5).

It is also interesting to compare results (given in Results of the simulations and discussion section) obtained by numerical computations of gasification represented by reaction 1 and 2 with results obtained by theoretical calculation of the equilibrium composition of the gas mixture in the reactor during gasification. The approach adopted for the calculations is based on the minimizing of total free energy of the system upon assumption of local thermodynamic equilibrium, which represents the basis of so called non-stoichiometric algorithm [18]. In the case of given pressure and temperature, as is the case of the results presented, the function to be minimized is the total Gibbs energy of the system within the domain of mass-balance constraints [18-20]. Because of the relatively low temperatures of the reacting mixture within the reactor it is necessary to regard the system as heterogeneous one. The approach adopted here is a subject of the paper [21] in which the computer program used for the calculations is described. Standard thermodynamic functions in the form of approximation coefficients [22] together with the corresponding standard enthalpy of formation of individual substances considered in the mixture serve as the input data and have been taken from the database system as the part of the computational suite for the calculations of composition and thermodynamic properties of the system in LTE [22].

The number of selected species in the temperature range 300-6000 K at pressure 1 bar is 122 including liquid water and condensed carbon. The initial amount of substances (in moles) are as follows: 0.446 C; 0.439 H; 0.4962 O; and 0.0059 N. These amounts correspond the experimental flow of the gases under assumption of homogenous mixing.

The main result of the calculation of composition of the system is that the condensed carbon is present in the system up to 1000 K which could be attributed the tendency of overestimation of abundance for more stable substances in the thermodynamic equilibrium against the composition of the kinetic driving processes. Second result is that there is a global maximum of mole fraction function on temperature of solid carbon. This maximum is approximately at 400 K and the value of the mole fraction at that temperature is $x_{(C(solid))}$=0.81. Mole fraction of solid carbon is defined for the purpose of composition calculation as a fraction of solid carbon amount to all species present only in gas phase amount. It is important to emphasize that there is no presence of carbon at all defined in reactions 1,2 in numerical simulations of gasification. The only solid substance possibly present in the reactor within computations of gasification is solid wood (wooden particles) that have not been volatilized by plasma flow. This means that it is not suitable to establish automatically a link between presence of solid wood and presence of solid carbon. Nevertheless such computation of equilibrium composition of the mixture in the reactor has its meaning as in experiment of gasification there is usually some amount of condensed carbon.

Computation of the equilibrium composition of the mixture for our specific mass flows in the reactor according to the description given above was carried out with use of already existing code by O. Zivny.

Governing equations

In all numerical computations presented in the thesis following transport equations are solved (Einstein summation rule is applied to all following equations):

Continuity equation

$$\frac{\partial}{\partial t}\rho + \frac{\partial}{\partial x_i}(\rho v_i) = S_m \qquad \text{(eq.13)}$$

Momentum conservation equation

$$\frac{\partial}{\partial t}\rho v_i + \frac{\partial}{\partial x_j}(\rho v_i v_j) = -\frac{\partial}{\partial x_i}p + \frac{\partial}{\partial x_j}\tau_{ij} + \rho g_i + F_i \qquad \text{(eq.14)}$$

Energy equation

$$\frac{\partial}{\partial t}(\rho E) + \frac{\partial}{\partial x_i}(v_i(\rho E + p)) = -\frac{\partial}{\partial x_i}(k_{eff}\frac{\partial}{\partial x_i}T - \sum_{k=1}^{N} h_k (J_k)_i + \tau_{ij} v_j) + S_h \qquad \text{(eq.15)}$$

Species transport equations

$$\frac{\partial}{\partial t}\rho Y_i + \frac{\partial}{\partial x_j}(\rho v_j Y_i) = -\frac{\partial}{\partial x_j}(J_i)_j + R_i + S_M \qquad \text{(eq.16).}$$

where ρ is the density of the fluid phase; v_i is the i^{th} component of velocity vector; S_m is the mass added to the continuous phase from the dispersed second phase (e.g. due to the vaporization of liquid droplets) and from any user-defined source; p is the pressure; τ_{ij} is the ij^{th} component of stress tensor;

Stress tensor used in (eq. 14) is defined as follows:

$$\tau_{ij} = \mu\left(\left(\frac{\partial}{\partial x_j}v_i + \frac{\partial}{\partial x_i}v_j\right) - \frac{2}{3}\frac{\partial}{\partial x_k}v_k I_{ij}\right) \qquad \text{(eq.17)}$$

μ is the molecular viscosity; I_{ij} is the ij^{th} component of unit tensor; g_i is i^{th} component of gravitational acceleration; F_i is i^{th} component of external body force (interaction with dispersed phase); E is the energy; k_{eff} is the effective conductivity defined as $k_{eff}=k+k_t$; where k is thermal conductivity and k_t is turbulent thermal conductivity defined according to standard k-ε model; T is the temperature; h_k is the enthalpy for chemical species k defined as follows:

$$h_k = \int_{T_{ref}}^{T} c_{p,k}\,dT \qquad \text{(eq.18)}$$

where T_{ref}=298.15 K; $c_{p.k}$ is the specific heat capacity at constant pressure for species k; $(J_k)_i$ is the i^{th} component of the diffusion flux for chemical species k; S_h is the sum of user defined volumetric heat sources and heat of chemical reaction; Y_i is the mass fraction of species i; $(J_i)_j$ is the j^{th} component of the diffusion flux for chemical species i; **J** as a diffusion flux is defined for species i in a vector form as follows:

$$\vec{J}_i = -\rho D_{i,m} grad Y_i - D_{T,i}\frac{gradT}{T} \qquad \text{(eq.19)}$$

where $D_{i,m}$ is the mass diffusion coefficient for species i in the mixture; $D_{T,i}$ is the thermal (Soret) diffusion coefficient R_i is the net rate of production of species i by chemical reactions.

Trajectory of solid particles is computed by following equation:

$$\frac{du_p}{dt} = F_D(u - u_p) + \frac{g_x(\rho_p - \rho)}{\rho_p} + F_x \qquad \text{(eq.20)}$$

where u is the fluid phase velocity; u_p is the particle velocity; term $F_D(u-u_p)$ is the drag force per unit particle mass; g_x is the gravitational acceleration in x direction; ρ_p is the particle density; $F_D$is defined as follows:

$$F_D = \frac{18 \mu C_D \mathrm{Re}}{24 \rho_p d_p^2} \quad \text{(eq.21)}$$

where μ is the molecular viscosity of the fluid; d_p is the instant diameter of the solid particle; C_D is the drag coefficient (dimensionless); Re is the relative Reynolds number: defined as:

$$\mathrm{Re} = \frac{\rho d_p \left| u_p - u \right|}{\mu} \quad \text{(eq.22)}$$

Transport equations for the standard k-ε model

The turbulence kinetic energy, k, and its rate of dissipation, ε, are obtained from the following transport equations:

$$\frac{\partial}{\partial t}(\rho k) + \frac{\partial}{\partial x_i}(\rho k u_i) = \frac{\partial}{\partial x_j}\left[\left(\mu + \frac{\mu_t}{\sigma_k}\right)\frac{\partial k}{\partial x_j}\right] + G_k + G_b - \rho\varepsilon - Y_M + S_k \quad \text{(eq.23)}$$

and

$$\frac{\partial}{\partial t}(\rho \varepsilon) + \frac{\partial}{\partial xi}(\rho \varepsilon u_i) = \frac{\partial}{\partial x_j}\left[\left(\mu + \frac{\mu_t}{\sigma_\varepsilon}\right)\frac{\partial \varepsilon}{\partial x_j}\right] + C_{1\varepsilon}\frac{\varepsilon}{k}\left(G_k + C_{3\varepsilon}G_b\right) - C_{2\varepsilon}\rho\frac{\varepsilon^2}{k} + S_\varepsilon \quad \text{(eq.24)}$$

In these equations, G_k represents the generation of turbulence kinetic energy due to the mean velocity gradients. G_b is the generation of turbulence kinetic energy due to buoyancy. Y_M represents the contribution of the fluctuating dilatation in compressible turbulence to the overall dissipation rate and in our case Y_M=0 because we model in the thesis incompressible flows only. $C_{1\varepsilon}$, $C_{2\varepsilon}$, and $C_{3\varepsilon}$ are constants. σ_k and σ_ε are the turbulent Prandtl numbers for *k* and ε, respectively. S_k and S_ε are user-defined source terms.

Modelling the Turbulent Viscosity and the Model Constants

The turbulent (or eddy) viscosity, μ_t, is computed by combining k and ε as follows:

$$\mu_t = \rho C_\mu \frac{k^2}{\varepsilon} \quad \text{(eq.25)}$$

where C_μ is constant.

The model constants $C_{1\varepsilon}$, $C_{2\varepsilon}$, C_μ, σ_k, and σ_ε have the following default values:
$C_{1\varepsilon}$=1.44, $C_{2\varepsilon}$=1.92, C_μ=0.09, σ_k=1.0, σ_ε=1.3

These default values have been determined from experiments with air and water for turbulent flows. They have been found to work fairly well for a wide range of wall-bounded and free shear flows. The default values of the model constants are the standard ones that are most widely accepted. More detailed description on this turbulence model is given in [5].

The term G_k represents the production of turbulence kinetic energy. From the exact equation for the transport of k, this term G_k may be defined as

$$G_k = -\rho\overline{u_i' u_j'}\frac{\partial u_j}{\partial x_i} \quad \text{(eq. 26)}$$

It is possible to evaluate G_k in a manner consistent with the Boussinesq hypothesis, and then we get $G_k=\mu_t S^2$ where S is the modulus of the mean rate-of-strain tensor, defined as

$$S = \sqrt{2S_{ij}S_{ij}} \qquad \text{(eq. 27)}$$

When a non-zero gravity field and temperature gradient are present simultaneously, the k-ε models account for the generation of k due to buoyancy (G_b in eq. 23), and the corresponding contribution to the production of ε in eq. 24.

The generation of turbulence due to buoyancy is given by

$$G_b = \beta g_i \frac{\mu_t}{\mathrm{Pr}_t} \frac{\partial T}{\partial x_i} \qquad \text{(eq. 28)}$$

where Pr_t is the turbulent Prandtl number for energy and g_i is the component of the gravitational vector in the i-th direction. For standard k-ε model the default value of Pr_t is 0.85. The coefficient of thermal expansion, β, is defined as

$$\beta = -\frac{1}{\rho}\left(\frac{\partial \rho}{\partial T}\right)_p \qquad \text{(eq. 29)}$$

Thermophoretic force is defined as

$$F_x = -D_{T,p} \frac{1}{m_p T} \frac{\partial T}{\partial x} \qquad \text{(eq.30)}$$

where $D_{T,p}$ is the thermophoretic coefficient. Thermophoretic force acts on particles suspended in gas phase that has non-zero temperature gradient and this force is of direction opposite to that of the gradient. This force is more obvious in case of smaller particles and it enters eq. 20 by the term F_x.

Results of the simulations and discussion

Results of all numerical simulations are mainly presented as images obtained from Ansys Fluent® code. These images show calculated distributions of relevant physical or chemical properties. The thermal plasma reactor do not possesses any axial symmetry (nor any other symmetry) and hence it was necessary to carry out 3 dimensional (3D) computations. On the other hand it is not practical to view 2D projections of 3D images all the time and so just results corresponding to 2D cuts of the reactor geometry are given in majority of cases. All simulations presented in this section are converged. Level of convergence for the case of 0.2 mm wooden particles is given in Fig. 15. In Table 10. the reached convergence level is given for all three investigated cases. Values given in Table 10. are valid for constant heat transfer coefficient boundary condition setting. Scaled residuals history presented in Fig. 15 is valid for both cases of boundary condition setting –for constant temperature boundary condition of 1300 K at all reactor walls and also for constant heat transfer coefficient boundary condition setting because at around 25000th iteration this boundary condition was changed from constant temperature to constant heat transfer coefficient. A numerical simulation is considered to be converged if all scaled residuals fall below the value of 10^{-3} and scaled residual for energy below the value of 10^{-6}. This is reached for majority of residuals in Table 10. For few residuals this value has not been met however they are very close to it. With respect to the fact that some residuals had been still little above the threshold values denoting full convergence the computations were continued and results repeatedly checked in order to verify if the solutions were constant with increasing number of iterations. Values of residuals entered in Table 10 are given in the form Y-Z that means $Y.10^{-z}$.

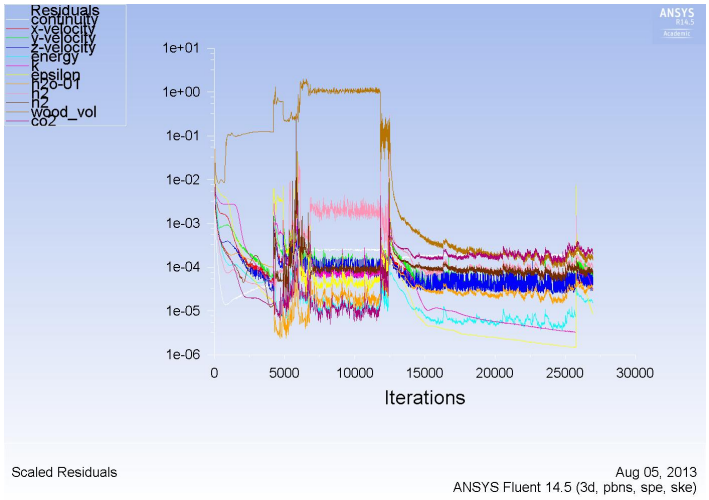

Fig. 15 Scaled residuals history
Mean particle diameter: 0.2 mm
26966 Iterations

Table 10
List of reached values of monitored residuals for all 3 investigated cases

Particle diameter	**Continuity**	**x-velocity**	**y-velocity**	**z-velocity**	**energy**	**k**
0.2 mm	2.1210-04	3.7015-05	5.0493-05	3.4710-05	1.5431-05	3.2321-05
2 mm	4.0948-04	9.3740-04	2.9721-04	1.2165-04	2.6901-05	1.2974-05
20 mm	4.5609-04	5.8510-04	8.3280-04	5.9787-04	2.4438-05	1.5828-05
	ε	**H_2O**	**H_2**	**N_2**	**Wood_vol**	**CO_2**
0.2 mm	8.9205-06	3.0417-05	1.0172-04	7.7493-05	1.6108-04	2.0922-04
2 mm	3.9747-06	3.6016-05	3.9736-04	2.8667-04	1.0713-04	2.9810-04
20 mm	1.6781-05	6.5900-05	8.4124-04	2.9549-03	7.6363-05	5.2238-04

Temperature distributions

The knowledge of temperature distributions is most important of all other distributions of other physical properties because temperature of the mixture directly determines the rate of chemical reactions and thus corresponding yield as it is given in Fig. 14. Converged solution for temperature distributions are given in Figs. 16-18. In this sequence of temperature distributions an extent of an

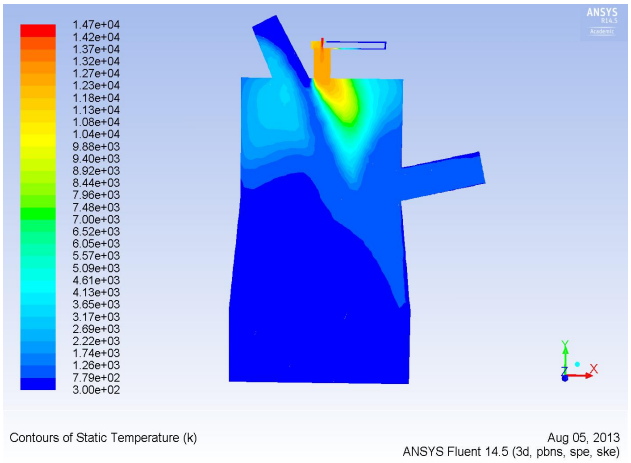

Fig. 16 2D Cut of Temperature distribution-global view
(Range: 300K-14700K)
Mean particle diameter: 0.2 mm

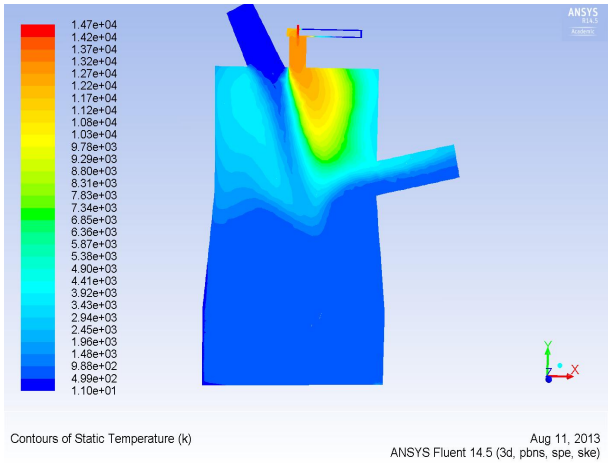

Fig. 17 2D Cut of Temperature distribution-global view
(Range: 300K-14700K)
Mean particle diameter: 2 mm

efficiency of mixing of thermal plasma flow with cold gas flow and with flow of solid particles is presented. All Figs. 16-18 show high temperature areas that are nearly independent on diameter of inflowing particles. These areas are always located for all three cases at the upper right corner of the reactor chamber. In real experiments such high temperature areas have a special purpose. These areas enable the unwanted products of chemical reactions to decompose before leaving the reactor. An other result following from Figs. 16-18 is that reactor chamber is not uniformly heated. At the upper parts of the reactor the temperature is higher and at lower parts on the contrary. This inhomogeneity is caused by energy drain of cold gas and cold solid particles injected through waste input as it is shown in Fig. 4. In Fig. 16 the level of temperature homogeneity is highest and it subsequently decreases with increasing diameter of gasified particles. This is caused by ability of particles to interact physically and chemically with hot plasma flow. Smallest particles have the largest ratio of particle surface to particle weight as surface increases with second power but weight increases with third power of radius. And with respect to the fact that it is just the surface of the particle that can interact with flow and that the number of smallest particles is highest of all (for constant overall mass flux of solid particles) the smallest particles can mix hot

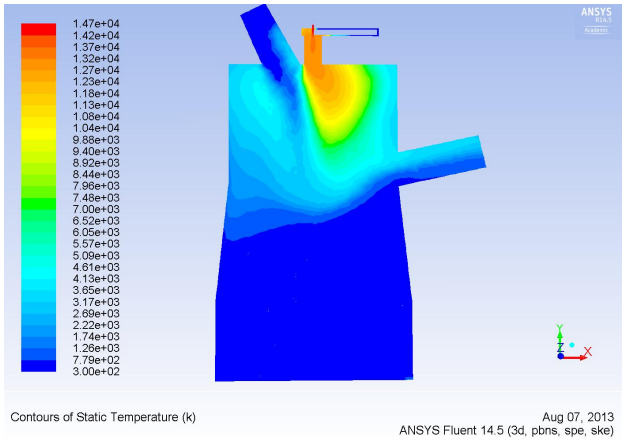

Fig. 18 2D Cut of Temperature distribution-global view
(Range: 300K-14700K)
Mean particle diameter: 20 mm

and cold flows together due to this more than that ones of higher diameter. Smaller particles are able to withdraw more heat energy from upper parts of the reactor and to carry it towards bottom of the reactor and so upper parts of the reactor are colder in case of smaller particles. This effect is more visible in Figs. 19-21. where red contour denotes the frontier of an area with temperature of 4000 K or higher. It means that temperatures higher than 4000 K are not displayed in these Figs. and so such areas are colourless. In the case of 20 mm particles that is presented in Fig. 19 we can see the largest colourless area what means largest accumulation of heat among all three cases. By simple comparison of an extent of these colourless areas we again obtain that best mixing occurs with the smallest particles and vice versa. Level of temperature homogeneity is not ideally visible in Figs. 16-18 and so a view containing more suitable temperature range is selected in Figs. 19-21. The mayor lower part of the reactor is heated to the temperature range from 670 K to 793 K as it is given in Fig. 19 while analogous part in Figs. 20-21 is heated only to the temperature range from 546 K to 670 K. Lower temperature range means lower mixing. In Fig. 20 there is at least some intrusion of higher temperature towards the investigated part of the reactor but in Fig.21 upper and lower parts of the reactor are separated most from temperature point of view. In Figs. 22-24 3D distribution of temperature inside of the reactor chamber is given. Since the computational grid is very dense we see in Figs. 22-24 mainly a distributions of temperature on inner reactor walls (representing the boundary of the computational domain). With respect to the fact that modeling presented in the thesis is focused mainly on reactor chamber the distributions of the jet and anode area are not given in Figs. 22-24. By comparison of Figs. 22-24 with Figs. 19-21 we see direct resemblance of 3D temperature distributions on the walls with corresponding 2D cuts of temperature distributions given in Figs. 19-21. Temperature range is the

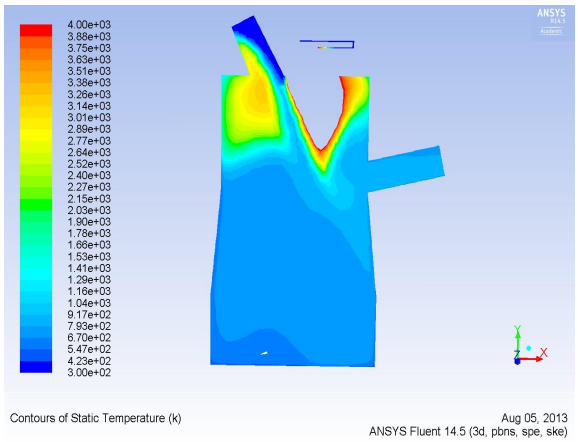

Fig. 19 2D Cut of Temperature distribution-global view (Range: 300K-4000K)
Mean particle diameter: 0.2 mm

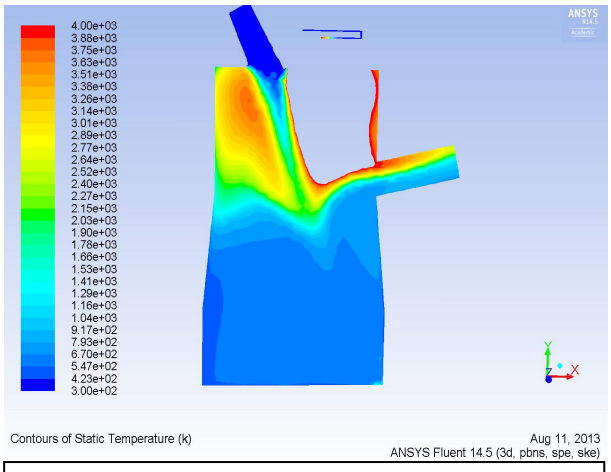

Fig. 20 2D Cut of Temperature distribution-global view (Range: 300K-4000K)
Mean particle diameter: 2 mm

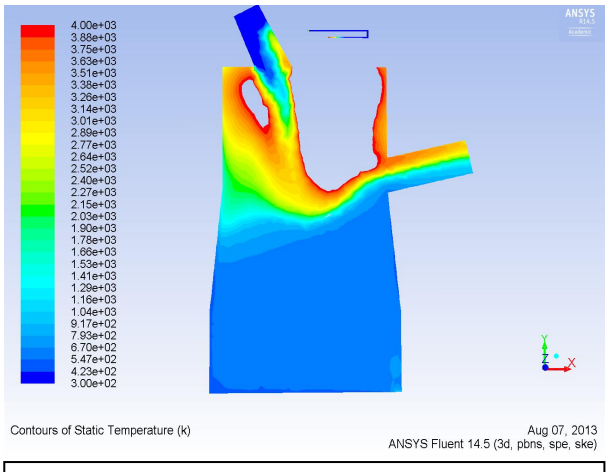

Fig. 21 2D Cut of Temperature distribution-global view (Range: 300K-4000K)
Mean particle diameter: 20 mm

same in Figs. 19-21 and also in Figs. 22-24 what makes the comparison easier. In Fig. 24 there is the largest hot area at the top of the reactor chamber of all three cases (marked by red colour) what indicates lowest flow mixing. This heat energy is then to some extent exhausted by exhaust pipe out of the ractor what is indicated by orange and yellow colour at the upper parts of the exhaust tube. This exhausting of heat energy is lower in Fig. 23 and lowest in Fig. 22. All these observations proves that mixing is better with decreasing diameter of the particles.

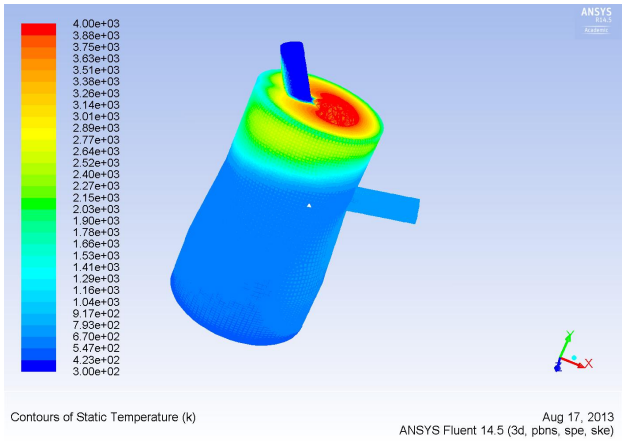

Fig. 22 3D Temperature distribution-global view
(Range: 300K-4000K)
Mean particle diameter: 0.2 mm

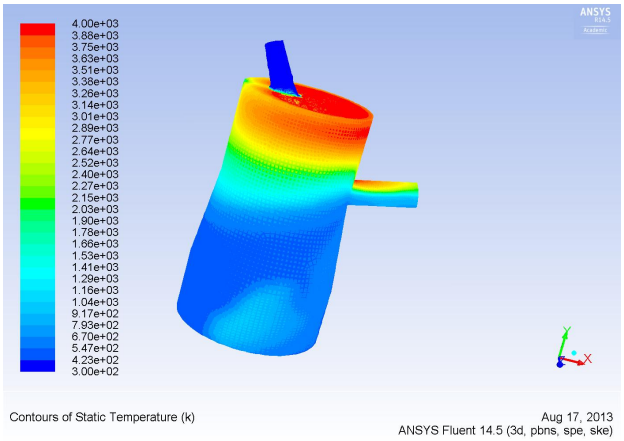

Fig. 23 3D Temperature distribution-global view
(Range: 300K-4000K)
Mean particle diameter: 2 mm

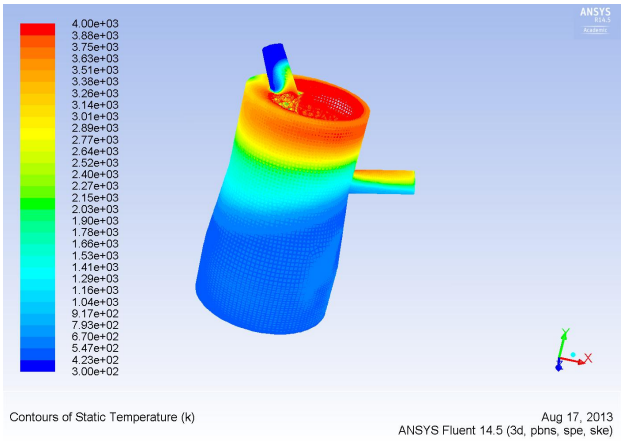

Fig. 24 3D Temperature distribution-global view
(Range: 300K-4000K)
Mean particle diameter: 20 mm

Distributions of mole fractions of chemical species

With average temperature high enough in all reactor chamber a products of chemical reactions begin to occur. Distribution of mole fraction of CO for all three case is given in Figs. 25-27. In this sequence a homogeneity dependency of mole fraction distribution of CO on particle diameter is visible again. The best result is given in Fig. 25 and worst in Fig.27. Experimental results for mole

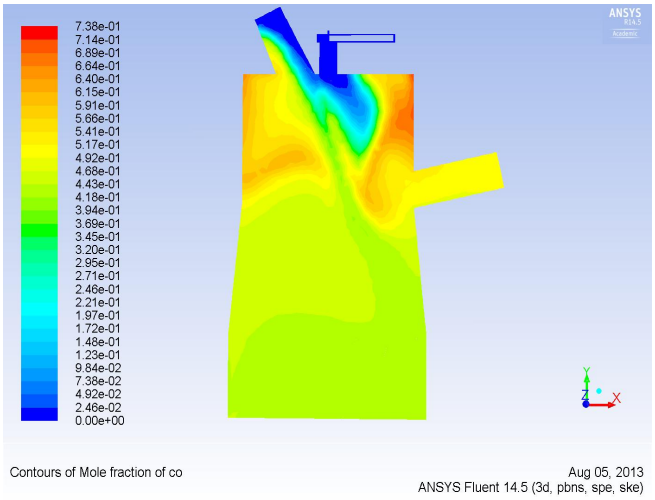

Fig. 25 2D Cut of Distribution of mole fraction of CO- global view (Range: 0-0.738 (dimensionless))
Mean particle diameter: 0.2 mm

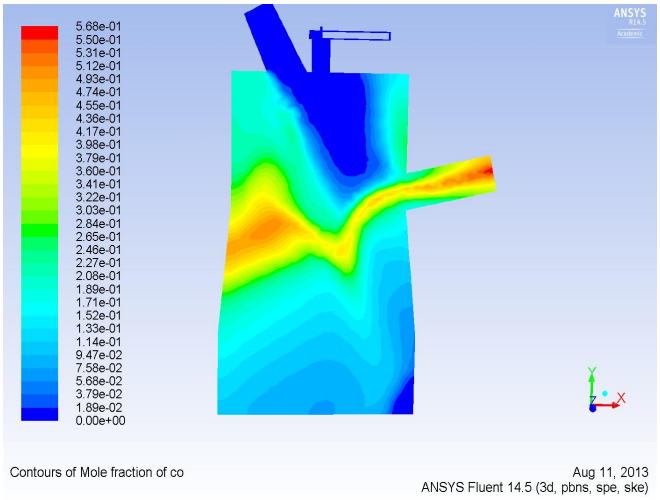

Fig. 26 2D Cut of Distribution of mole fraction of CO - global view (Range: 0-0.568 (dimensionless))
Mean particle diameter: 2 mm

fraction of CO at the reactor exit is 60% and theoretical result obtained by numerical simulation is 55% for 0.2 mm particles; 52% for 2 mm particles and 48% for 20 mm particles. These numerical results do not fit exactly the experimental value for CO but they are close to it. It is important to mention that regardless of mixing efficiency of plasma flow with cold flow of gas and particles the final result of gasification at the reactor exit is nearly the same. In Figs. 28-30 an analogous results for H_2 are given. Experimental value of molar fraction of H_2 is 30% and in these theoretical computations they are 27% for 0.2 mm particles; 25% for 2 mm particles and 22% for 20mm particles. In case of 0.2 mm particles the mixing and thus chemical reactions occur more or less in majority of the reactor chamber and thus the reaction yield is high. In cases of 2mm and 20 mm particles the mixing is much worse but still the reaction yield is relatively good. This is because in both this cases a thin reaction layer is created in the middle of the reactor chamber. In these two cases chemical reactants (CO_2; steam plasma and wood volatiles) are demixed to a significant extent. Steam plasma and CO_2 remain in the upper side of the reactor chamber and wood volatiles occupy lower part of the reactor chamber. All these

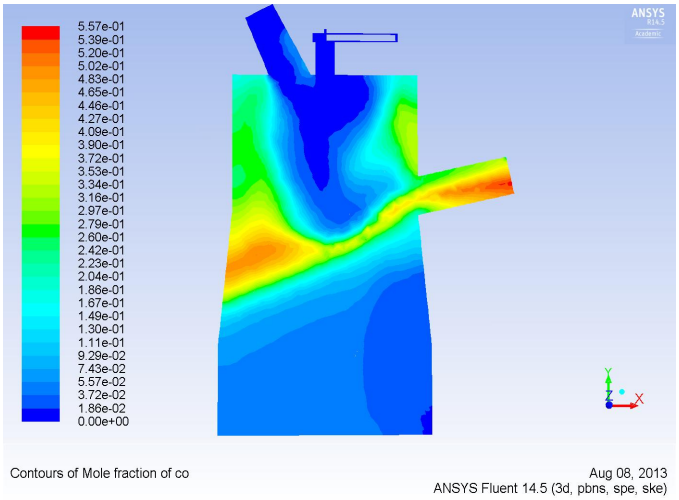

Fig. 27 2D Cut of Distribution of mole fraction of CO - global view (Range: 0-0.557 (dimensionless))
Mean particle diameter: 20 mm

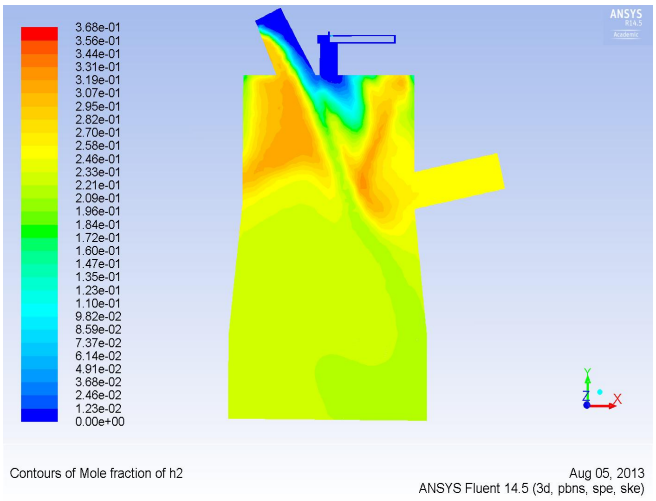

Fig. 28 2D Cut of Distribution of mole fraction of H_2-global view (Range: 0-368 (dimensionless)) Mean particle diameter: 0.2 mm

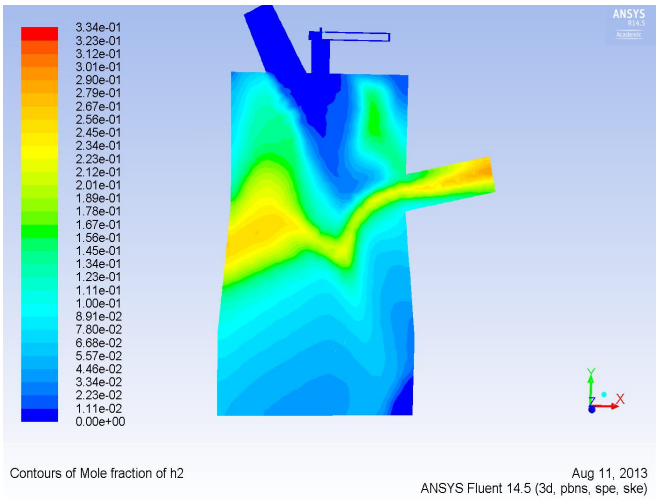

Fig. 29 2D Cut of Distribution of mole fraction of H_2 - global view (Range: 0-0.334 (dimensionless)) Mean particle diameter: 2 mm

reactants meet in the middle part of the reactor creating the reaction layer. In these two cases both chemical reactions occur practically in the reactor layer only. Since reaction yields in these both cases are still relatively good the rates of chemical reactions as defined in Table 8 are obviously high enough in comparison to macroscopic physical flow of plasma and cold gases. Technically speaking although reaction yield decreases with increase of particles diameter it is still high enough to say that process of gasification and syngas production is effective. Thus a global result of these computations is that all three investigated diameters of solid particles are suitable for use in the reactor since we do not primarily follow efficiency of mixing itself but just final reaction yields. All these computations were carried out implementing a heat transfer to the reactor walls determined by constant heat transfer coefficient as it was described in computing procedure chapter. However it is interesting to investigate a case with all parameters remained but with boundary condition changed to constant temperature of 1300 K. Results for this case are given in special case with constant temperature boundary condition chapter. Results containing distributions of mole fractions of other chemical species are not given here because they just reflect distributions of species already presented.

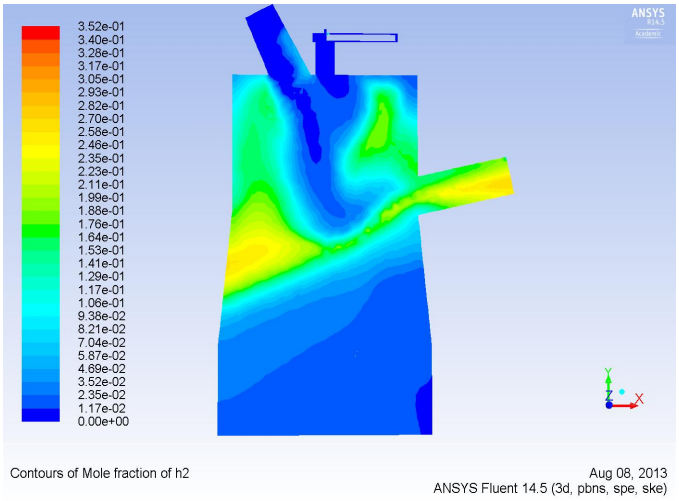

Fig. 30 2D Cut of Distribution of mole fraction of H_2-global view (Range: 0-0.352 (dimensionless)) Mean particle diameter: 20 mm

Velocity distributions

In this section in all figures only 2D cuts of distribution of velocity magnitudes (absolute values of velocity vectors) are presented for all three investigated cases. This sequence shows us an areas

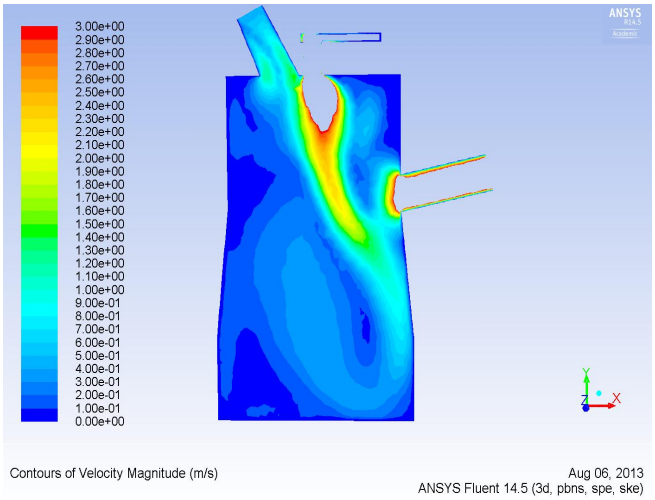

Fig. 31 2D Cut of Distribution of velocity magnitude- global view (Range: 0-3 m/s) Mean particle diameter: 0.2 mm

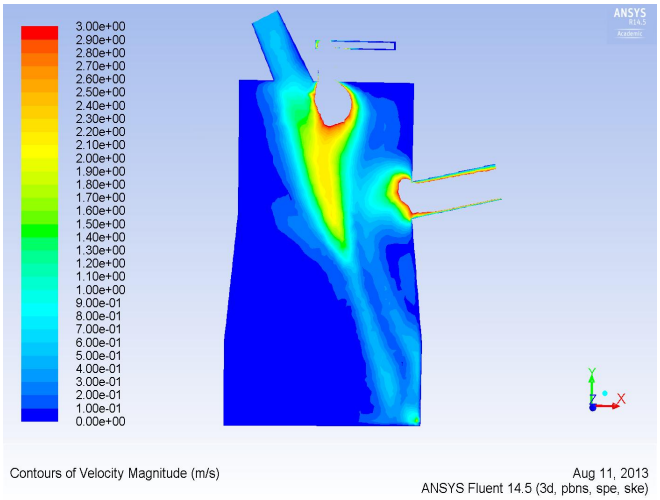

Fig. 32 2D Cut of Distribution of velocity magnitude- global view (Range: 0-3 m/s)) Mean particle diameter: 2 mm

where the main (prevailing) flow occurs and also its magnitude. In majority of reactor chamber in all the cases the flow is slower than 3 m/s. Colourless areas again denote areas of velocity higher than 3 m/s. Mobility of the gas mixture depends again on particles diameter. Highest average velocities are reached in case of 0.2 mm particles. In case of 0.2 mm particles the main flow turns left (as seen from viewer`s point of view) after reaching the bottom of the reactor and then it rises up towards areas with higher temperatures what is ideal because reactants in such a flow will have enough time to undergo chemical reactions in order to produce high reaction yield. In case of 2 mm particles the main flow turns right towards exhaust pipe what means less time for reactants before being exhausted. And in case of 20 mm particles we see that the flow is practically discontinued at the middle of the reactor what means that CO_2 injected through waste input pipe remains in the upper part of the reactor and is also partially exhausted out of the reactor. And solid particles that are injected together with CO_2 fall down only due to the gravity towards right bottom corner of the reactor where they are volatilized. Volatilized wood occupy all lower half of the reactor and it flows up only due to increase of partial pressure of wood volatiles that is caused purely by continuous gain of solid

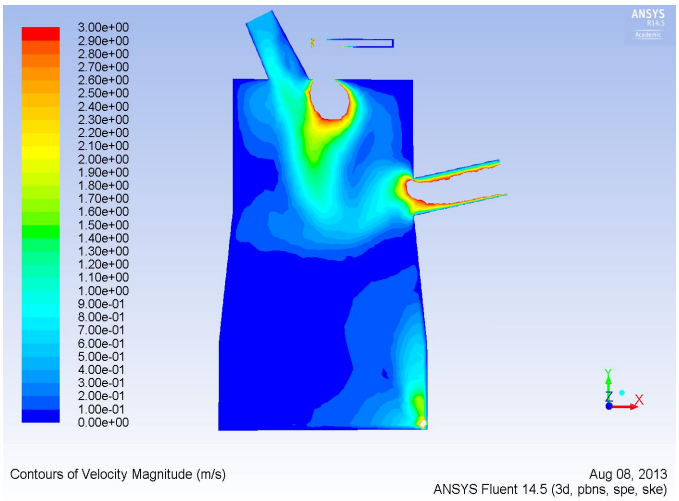

Fig. 33 2D Cut of Distribution of velocity magnitude -global view (Range: 0-3 m/s) Mean particle diameter: 20 mm

wood and hence by gain of wood volatiles in the area.

Velocity vectors

Distributions of velocity vectors presented as 2D cuts of the reactor given in Figs. 34-39 show that direction of the main stream is mainly within the xy-plane. Figs. 34-36 are focused on upper part

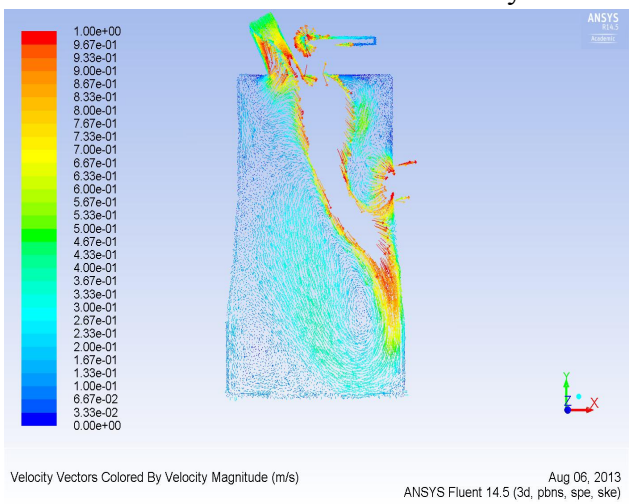

Fig. 34 Velocity vectors-global view
(Range: 0-1 m/s)
Mean particle diameter: 0.2 mm

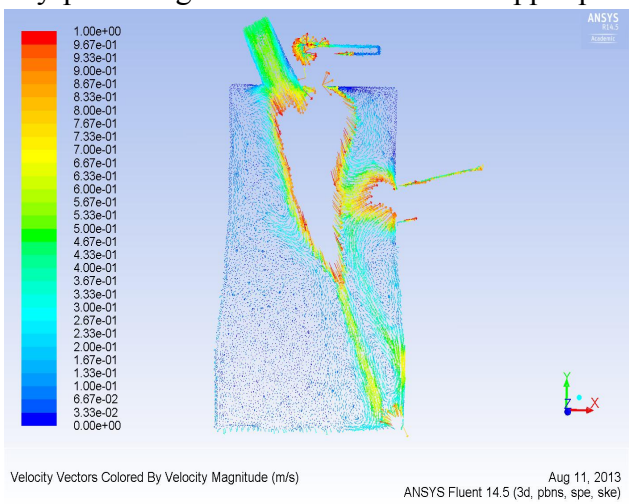

Fig. 35 Velocity vectors-global view
(Range: 0-1 m/s)
Mean particle diameter: 2 mm

of the reactor where colourless area indicates speeds higher than 1 m/s. Because of practical reasons the displayed velocity range is limited to 1 m/s in all figures presented in this section. Situation at bottom right corner of the reactor is given in Figs. 37-39 where detailed look at velocity vectors is presented while the scale is kept unchanged. Most widespread flow (it means flow of velocities around maximum displayed value) is in case of the smallest particles. In case of 2 mm particles there is still visible a main stream at bottom right corner but it is smaller and turned to the right side after reaching the bottom of the reactor. On the other hand in case of 20 mm particles the main stream ends at the middle part of the reactor chamber and then it flows out towards the exhaust pipe. Below this part solid particles are driven mainly due to gravitational force and they flow towards the right bottom corner where they are being volatilized. These particles are also volatilized continuously during their motion through the reactor after being injected into the reactor but since these particles are too big they are volatilized for the most part in this corner. Flow that is observable at the corner is caused by temperature volume increase of volatilized wood that is created from solid particles. Nearly all solid particles that reach bottom of the reactor are transformed into wood volatiles. According to these results it is possible to make an assumption that for any bigger particles (with technically realizable

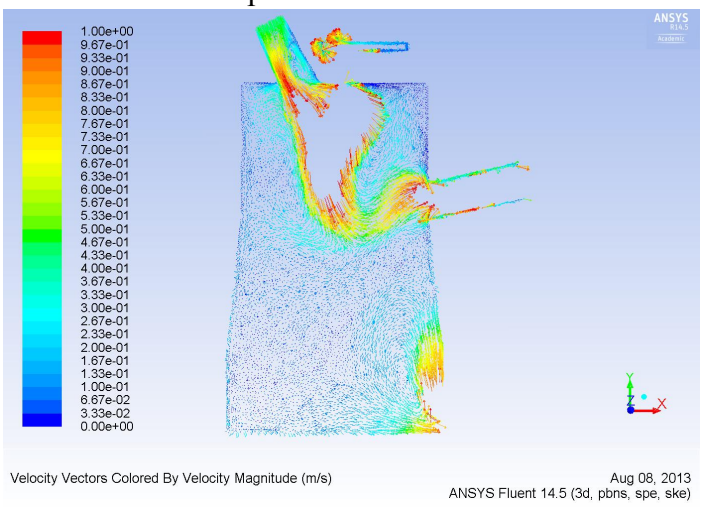

Fig. 36 Velocity vectors-global view
(Range: 0-1 m/s)
Mean particle diameter: 20 mm

diameter value according to our experiment setup) the distribution of physical properties would be very similar to these obtained for 20 mm particles. However some solid particles never reach the bottom of the reactor and they are exhausted out with just minor state of volatilization as it is given in separate chapter dedicated to discrete phase. In Figs. 37-39 there are also areas that are not affected by main stream. In such areas we can see that the flow there is very slow and it also do not follow xy plane only. Distributions of velocity vectors in Figs. 37-39 corresponds to distributions of velocity magnitudes presented in Figs. 31-33 (more specifically to the bottom right corner of Figs. 31-33).

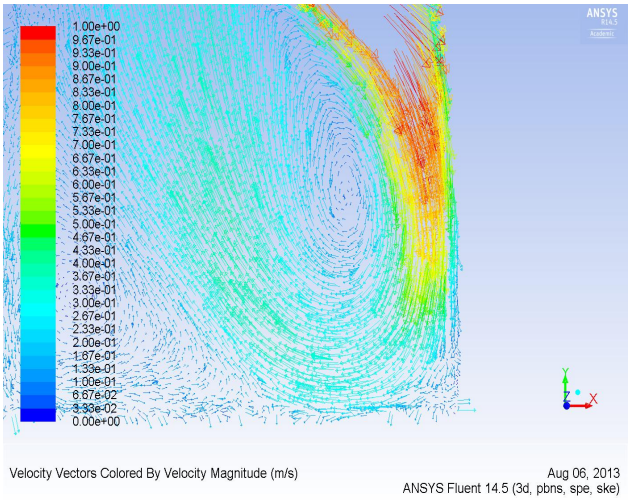

Fig. 37 Velocity vectors-bottom of the reactor
(Range: 0-1 m/s)
Mean particle diameter: 0.2 mm

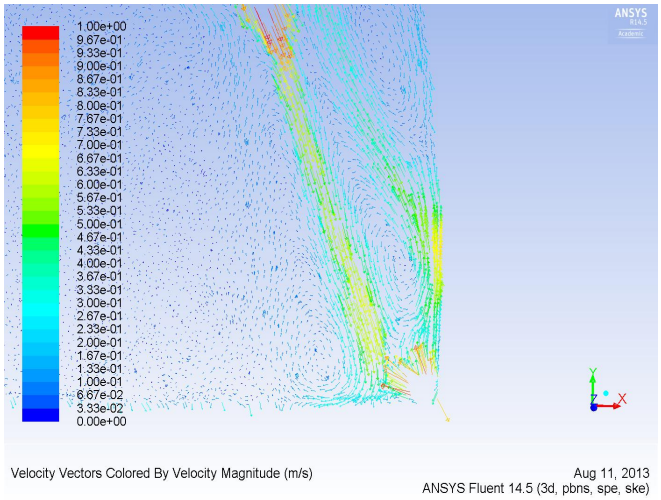

Fig. 38 Velocity vectors-bottom of the reactor
(Range: 0-1 m/s)
Mean particle diameter: 2 mm

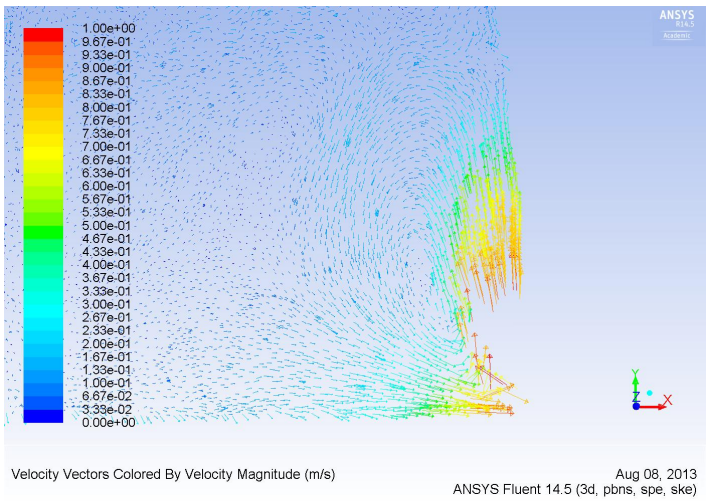

Fig. 39 Velocity vectors-bottom of the reactor
(Range: 0-1 m/s)
Mean particle diameter: 20 mm

Discrete phase distributions

Distribution of discrete phase is presented in Figs. 40-44 by distribution of concentration of solid wood. Results presented in Figs. 40-44 are very clear. In Fig. 40 the concentration of solid wood decreases rapidly as the flow of solid particles continuously passes through the reactor. In case of 0.2

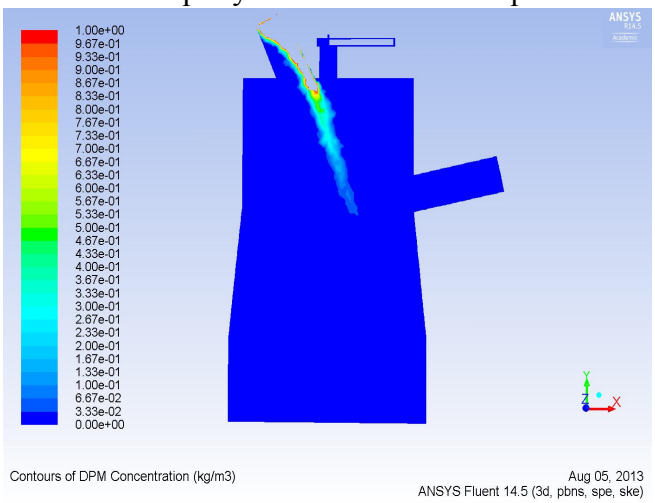

Fig. 40 2D Cut of Concentration of solid wood-global view (Range: 0-1 kg/m^3)
Mean particle diameter: 0.2 mm

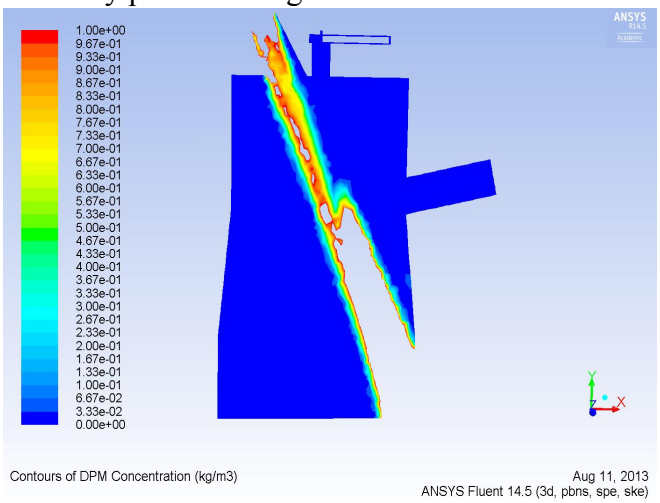

Fig. 41 2D Cut of Concentration of solid wood-global view (Range: 0-1 kg/m^3)
Mean particle diameter: 2 mm

mm particles all solid particles ale volatilized before entering middle part of the reactor. In case of 2 mm particles some particles (especially smaller ones) are volatilized but majority of such particles reach the bottom of the reactor but non of them escape through exhaust tube out of the reactor. In case of 20 mm particles we see that majority of the particles reaches the bottom and also that about 5% of the mass of solid particles escape from the reactor. Volume occupied by solid particles is not properly visible in Figs. 40-42 because density of solid wood used in the computations is 700 kg/m^3 as it is given in Table 6 and density interval used in Figs. 35-37 ranges only from 0 to 1 kg/m^3 in order to achieve fine display of the distribution. To remedy this a wider interval of values ranging from 0 up to 10 kg/m^3 was chosen in Figs. 43-44 where it is visible that only small volume is occupied by solid phase in these two cases. With respect to the limit of just 10 kg/m^3 it is possible to say that solid phase can be neglected from volumetric point of view. For a broader range like 0-100 kg/m^3 solid particles represent only a very small bubble at the right bottom corner of the reactor.

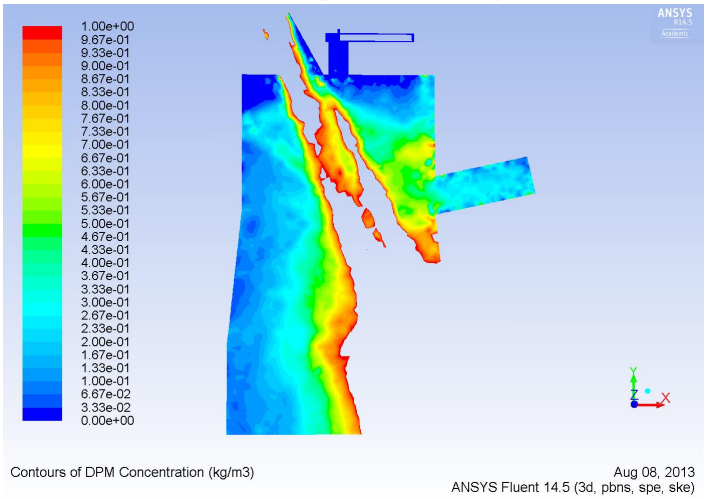

Fig. 42 2D Cut of Concentration of solid wood-global view (Range: 0-1 kg/m^3)
Mean particle diameter: 20 mm

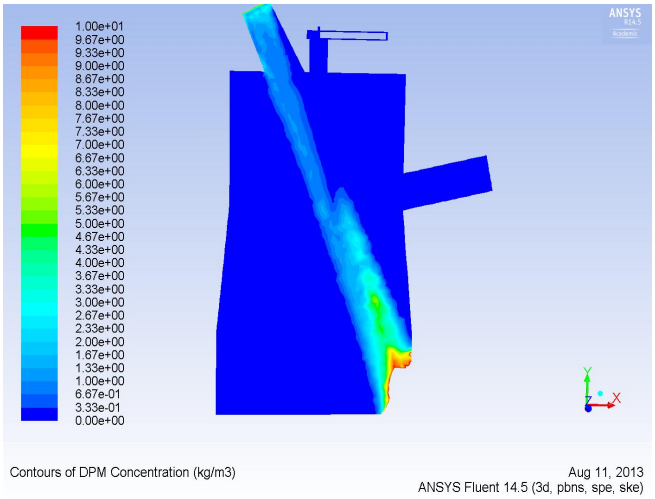

Fig. 43 2D Cut of Concentration of solid wood
(Range: 0-10 kg/m^3)
Mean particle diameter: 2 mm

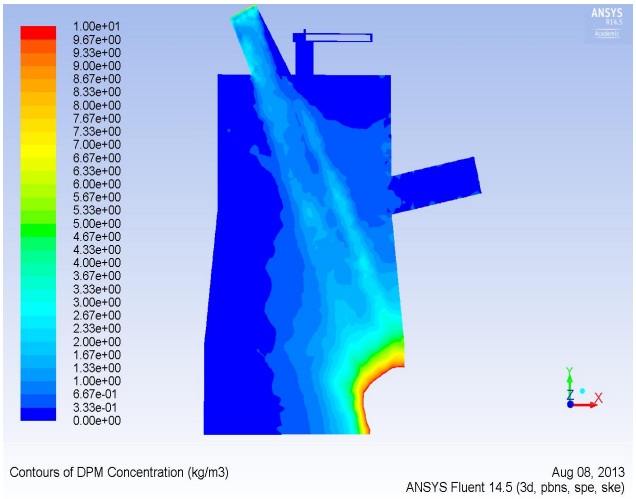

Fig. 44 2D Cut of Concentration of solid wood
(Range: 0-10 kg/m^3)
Mean particle diameter: 20 mm

Special case with constant temperature boundary condition

It is interesting to investigate a special case of gasification setting where namely a constant boundary condition for temperature is set for all inner reactor walls. All other boundary parameters and gasification setting remain the same as they are set above. The final temperature for the computation for walls was set to 1300 K. This value follows from experimental measurements of reactor walls temperature during process of gasification. Typical results of such measurements are given in Fig. 45. The walls temperature is measured by a set of thermometers located at different positions at the reactor walls and hence a bunch of curves are obtained as a result as seen in Fig. 45. Computation presented in this subsection is also converged with history of scaled residuals nearly identical to those given in Fig. 15. Yellow peak of the epsilon residual in Fig. 15 located around 25000th iteration for the 0.2 mm particles denotes the change in the computation setting when

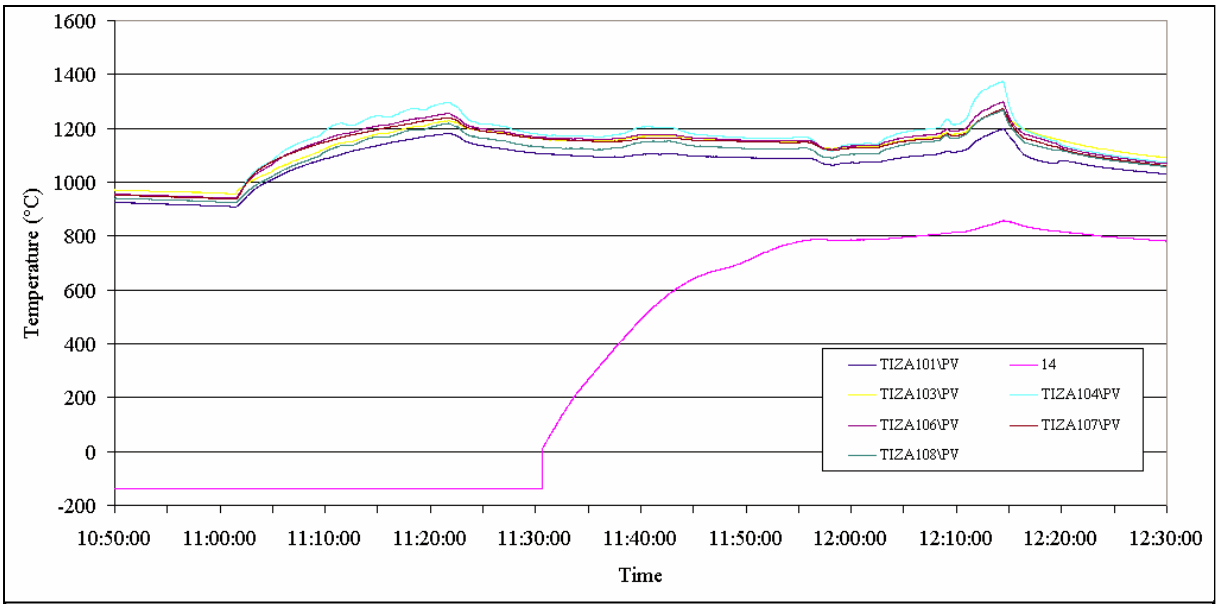

Fig. 45 Time dependence of reactor wall temperatures during process of gasification

constant temperature boundary condition was changed to the prescribed heat flux to the walls via constant heat transfer coefficient. This peak is small and all disturbed residuals fell down quickly. History of scaled residuals for case of 2 mm particles with such change of boundary condition is similar.

The aim of this subsection is to find out the influence of such setting on gasification of particles of 2 mm mean diameter. In sections above in all three cases the wall temperature of the reactor was calculated according to the actual and local temperature conditions in cells adjacent to the wall what can give highly non constant profile of temperature. Such wall temperature obtained from the computation can be lesser at the bottom of the reactor in comparison to experimental values what can lower the rate of chemical reactions or lower the rate of volatilization at such area resulting in lower yield of reactions at the reactor exit. Basic results of numerical simulations employing constant temperature boundary condition are given in Figs. 46-51. Distribution of temperature is more homogeneous in Figs. 46-47 in comparison to the case employing simulation of heat transfer to the walls via prescribed constant heat transfer coefficient as presented in Fig. 17 and Fig. 20. Lower parts of the reactor (comparable to the areas of the reactor heated up to the temperature range 546 K-670 K that is valid for 2 mm mean diameter of particles as it is given in Fig. 20) are heated to

temperature range 546 K-916 K. This means that at certain part of the area the temperature is higher what result to better mixing and higher rate of chemical reactions. This higher temperature in lower part of the reactor is caused by thermal heating of the gas mixture by reactor walls what can be seen in Fig. 47 where temperature close to the reactor wall in the bottom left corner is higher than it is in the middle of this part of the reactor. Bottom of the reactor chamber together with reactor walls between exhaust pipe and bottom of the reactor in fact heat the lower internal volume of the reactor by additional heat power input of 7.7 kW. This is the reason why distributions of physical properties are more homogeneous as it is given in Figs. 46-51 in comparison to the results valid for constant heat transfer coefficient boundary condition for the same mean particle diameter given in Figs. 17;20;26;29 and the like. On the other hand overall heat flux to all reactor walls is balanced in this case in a sense of fulfilling the constraint of 22 kW heat losses to the reactor walls. This means that in some sense the constant temperature boundary condition helps to transfer heat along vertical reactor walls. Results obtained for this case proves that this modeling of gasification is sensitive to boundary conditions changes. Other results for distribution of chemical species and solid wood are given in Figs. 48-51. In Fig. 48 there is more homogeneous distribution of mole fraction of CO than it is in analogous case in Fig. 26 what results to higher final yield of this species at the reactor exit - 56%.

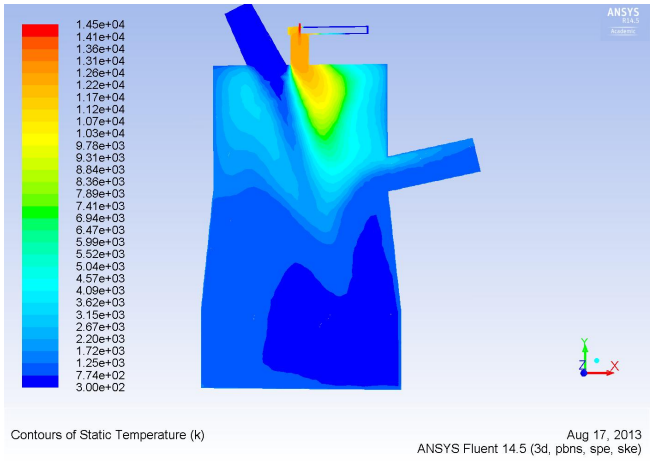

Fig. 46 2D Cut of Distribution of temperature
(Range: 300-14500 K)
Mean particle diameter: 2 mm

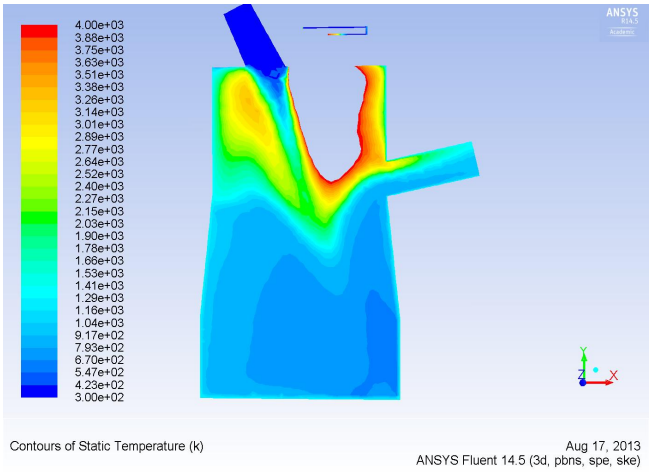

Fig. 47 2D Cut of Distribution of temperature
(Range: 300-14500 K)
Mean particle diameter: 2 mm

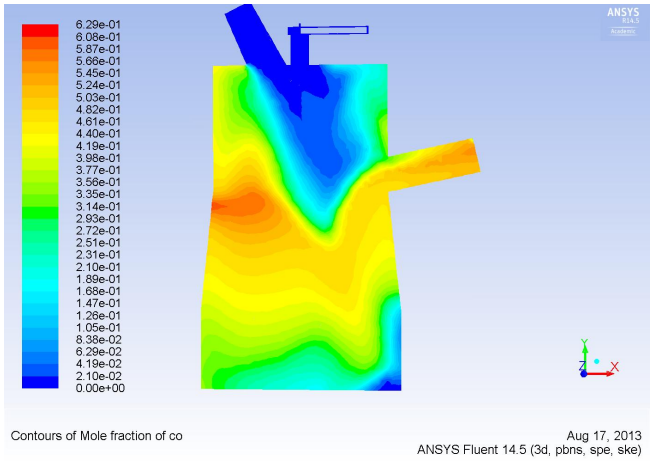

Fig. 48 2D Cut of Distribution of mole fraction of CO (Range: 0-0.629 (dimensionless))
Mean particle diameter: 2 mm

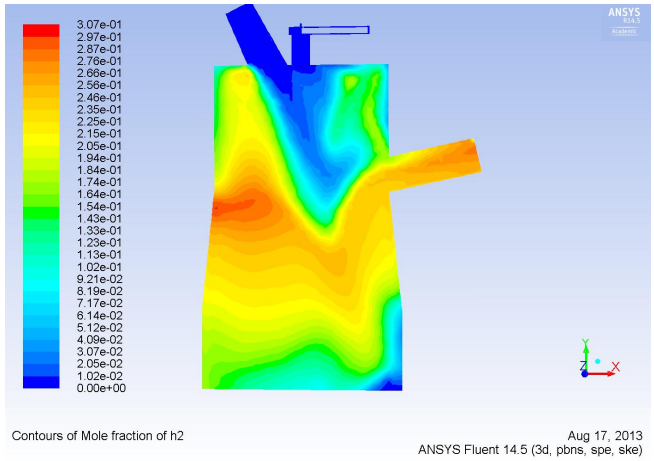

Fig. 49 2D Cut of Distribution of mole fraction of H_2 (Range: 0-0.307 (dimensionless))
Mean particle diameter: 2 mm

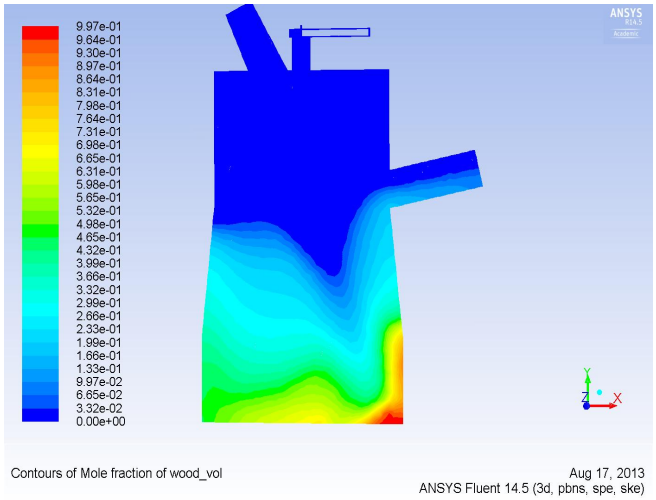

Fig. 50 2D Cut of Distribution of mole fraction of wood volatiles (Range: 0-0.997 (dimensionless))
Mean particle diameter: 2 mm

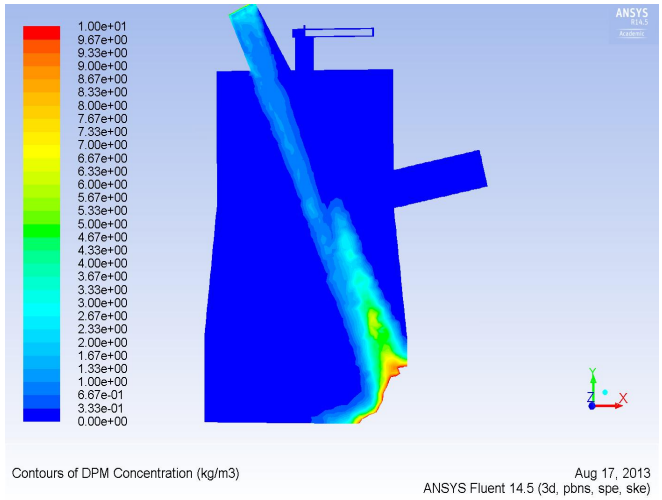

Fig. 51 2D Cut of Distribution of Concentration of solid wood (Range: 0-1 (dimensionless))
Mean particle diameter: 2 mm

Backflow of syngas

In the past the backflow of syngas from reactor chamber towards the anode area was verified by several more simple numerical simulations of gasification of wood. These verifications of backflow were based on computed presence of chemical species that were injected into the reactor chamber only and that were subsequently also found at the anode area after converged solution had been reached as it is given in [6]. Even older simulations proved the backflow by calculating the composition of gas mixture at the anode area and also by calculating vectors of velocity of gas mixture that were in the result of the opposite direction of the main prevailing flow as it is given in [1]. In calculations presented in the thesis both aspects are presented as a verification of backflow. In Fig. 52 the distribution of mole fraction of CO at the anode area is given. CO was chosen as an example of chemical species that are being produced in the reactor chamber only and hence it should not be present at anode or arc area. According to Fig. 52 the typical mole fraction of CO at the top of the anode is 0.00085%. This is low value at the first sight but during long-term operation of the torch and reactor this backflow leads to char formation at the anode surface. Such char in this area was also observed experimentally. Results for 2 mm and 20 mm particle diameters are very similar to the 0.2 mm particle diameters case and so they are not presented here. The differences concerning gas backflow among these three investigated cases is much smaller than the differences among distributions of temperature or mole fractions of species in the reactor chamber.

In the case of 0.2 mm particle diameters the results concerning the backflow of gas valid for H_2 are analogous complementary to the distribution of CO in the anode and arc area and so they are not presented as well.

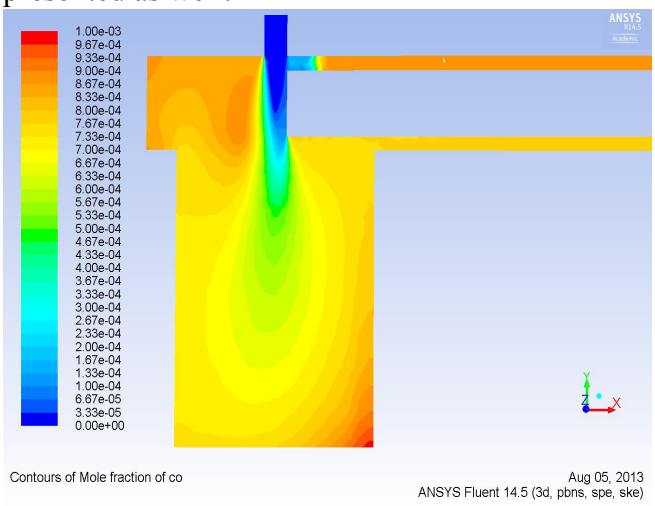

Fig. 52 2D Cut of Contours of Mole fraction of CO-Anode area (Range: 0-0.001)
Mean particle diameter: 0.2 mm

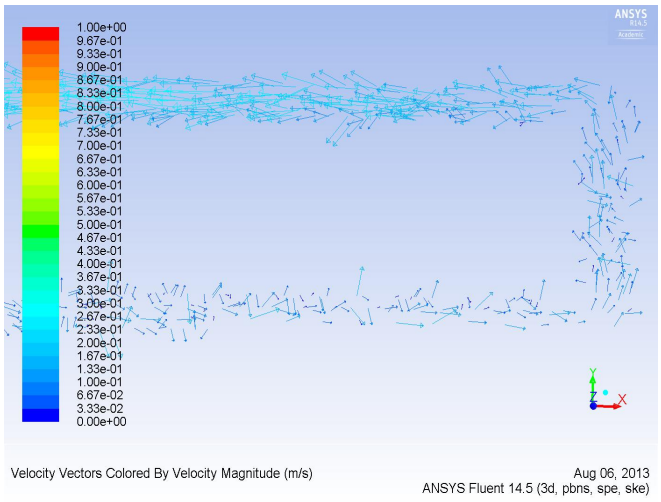

Fig. 53 2D Cut of Velocity vectors-Anode area (Range: 0-1 m/s)
Mean particle diameter: 0.2 mm

In Fig. 53 velocity vectors are displayed. The average speed of gas mixture in this anode area is low and approximately equals 0.05 m/s. This speed is higher at the top of the anode area and it also increases with decreasing of distance from plasma jet that operates here also as a pump that accelerates the gas. The gas at the anode area (and mainly above the anode) is accelerated by the "pump effect" of the jet regardless of lower temperature that is present at the vicinity of the jet above the anode.

Conclusion

The results of numerical computations presented in the thesis give relatively good approach to real physical and chemical processes of the gasification of wooden particles in the reactor chamber. This relative accuracy is evaluated according to reached scaled residuals (given in Table 10) that give information how much different is the $(N-1)^{th}$ iteration in comparison to N^{th} iteration and according to the yield of syngas and other chemical species at the end of the exhaust pipe of the reactor. This yield is compared with experimental values. Results given in the previous chapter say that efficiency of gasification and syngas production slowly decreases for increasing diameter of used particles. However this dependence is relatively slow and even for biggest investigated particles the reaction yield is still within 10% difference from experimental value. Lower yield of syngas for cases of bigger particles is caused both by lower total transfer of heat to bigger particles (what is caused just by shorter time such particles have for an interaction with plasma flow) what causes some amount of heat energy to be released out of the reactor without proper utilization of such heat energy and by the fact that some small amount of particles are exhausted prior to complete volatilization.
An other important result is the verification of backflow of gases from the reactor chamber towards anode area. This backflow is observed experimentally and it causes unwanted condensation of carbon at this area. This condensation in anode area is also verified by the computation of equilibrium composition of mixture used in the reactor (as described in Description of chemical processes of the gasification of wood section) since temperature of the outer side walls of the anode is low (approx. 700 K) due to well water cooling.

Distributions of physical properties around the plasma arc and upper parts of the plasma jet are not exact because only some features of real plasma arc were modelled here. On the other side these inaccuracies of arc modelling do not have significant influence on global yield of syngas production. If the diameter of particles is small enough particles are completely volatilized before reaching the bottom of the reactor and so defined chemical reactions of syngas production are volumetric what means now that these reactions occur in relatively large volume of the reactor. If the diameter of the particles is larger particles are only partially volatilized before reaching the bottom of the reactor during their motion after they were injected into the reactor. In such case chemical reactions occur in a relatively thin layer that is located in the middle of the reactor at the level where the exhaust pipe is connected to the reactor. This means that diameter of particles has big influence on distribution of physical properties inside the reactor chamber but the reaction yield is effected just a little.

It is not possible to model numerically every physical or chemical phenomena that exist in real experiment. It is mainly because the number of various effects is very high, the input parameters are unfortunately never exact – and this is now the biggest problem especially in determination of the rate of chemical reactions (rate exponents). Some parts of the model can be enhanced in the future. For example number of chemical reactions can be increased in order to simulate formation of solid carbon or it would be suitable to include at least some simple description of radiation and adsorption since temperature is high enough. Although the amount of energy carried by radiational effects is low at temperatures present in majority of the reactor volume the presence of such radiational model can bring better level of mixing of the mixture as a result because as it was shown in case of boundary condition changes the flow and gasification behaviour is sensitive to changes of certain type.

References

[1] I. Hirka, M. Hrabovsky, *"Three-Dimensional Modelling of Mixing of Steam Plasma Jet with Nitrogen in Thermal Plasma Reactor". in High Temperature Material Processes, 1-8, Volume 14, Issue 1, 2010*

[2] Joungmo Cho, Jeffrey M. Davis and George W Huber. *"The Intrinsic Kinetics and Heats of Reactions for Cellulose Pyrolysis and Char Formation". in: ChemSusChem, Volume 3, Issue 10, Article first published online: 16.AUG.2010.* (http://onlinelibrary.wiley.com/doi/10.1002/cssc.201000119/pdf)

[3] R. S. Miller and J. Bellan. *"A Generalized Biomass Pyrolysis Model Based on Superimposed Cellulose, Hemicellulose and Lignin Kinetics". in:Proc. 3rd International conference on combustion technologies, Vol 126, p. 97* (1997).

[4] B. F. Magnussen and B. H. Hjertager. *"On mathematical models of turbulent combustion with special emphasis on soot formation and combustion". In 16th Symp. (Int'l.) on Combustion*. The Combustion Institute. 1976.

[5] B. E. Launder and D. B. Spalding. *Lectures in Mathematical Models of turbulence.* Academic Press, London, England, 1972

[6] S. Janssens. *"Modeling of heat and mass transfer in a reactor for plasma gasification using a hybrid gas-water torch." M.Sc. Thesis,* Ghent University, Belgium, 2006-2007

[7] M. Hrabovsky, M. Konrad, V. Kopecky, M. Hlina, T. Kavka, G. Van Oost, B. Defoort, E. Beeckman, *"Gasification of biomass in water/gas-stabilized plasma for syngas production". in:Czechoslovak Journal of Physics, Vol.56* (2006)*, Suppl. B*

[8] G. Van Oost, M. Hrabovsky, V. Kopecky, M. Konrad, M. Hlina, T. Kavka, O. Chumak, E. Beeckman, J. Verstraeten. *"Pyrolysis of waste using a hybrid argon-water stabilized torch". Vacuum, 80, 1123-1137,* 2006

[9] J. Jenista. *"Numerical Modeling of Hybrid Stabilized Arc with Uniform Mixing of Gases". In: IEEE Transactions on plasma science, Vol. 32, NO. 2,* April 2004

[10] J. Jeništa *"Parameters of a Water-Vortex Stabilized Electric Arc Calculated by Using Different Radiation Models"*. Proc. of the 19th Symp. on Plasma Physics and Technology (CD-ROM, 281-284), Prague, June 6-9, 2000. Czechoslovak Journal of Physics 50 (Suppl. S3), 281-284, 2000.

[11] Chumak O., Kavka T., Hrabovský M.: *"Effect of anode attachment on structure and stability of plasma jet generated by dc arc torch"*. 18th International Symposium on Plasma Chemistry Abstract and Full-Paper CD. Kyoto : International Plasma Chemistry Society, 2007 - (Tachibana, K.; Takai, O.; Ono, K.; Shirafuji, T.) S. 1-4. ISBN 978-4-9903773-2-8. [CZ] [Anotace]

[International Symposium on Plasma Chemistry/18th./. Kyoto (JP), 26.08.2007-31.08.2007]

[12] Chumak O., Kopecký V., Konrád M., Kavka T., Hrabovský M.:*"Effect of pressure on behavior of anode attachment of dc arc plasma torch"*.In: High Temperature Materials and Processes **9** [3] (2005) 391-400. [CZ] [Anotace]

[13] Rutberg P. G., Bratsev AN, Ufimtsev AA, Plasmochemical technologies for processing of hydrocarbonic raw material with syngas production, J. of High Temp. Mat. Process. 8 (2004), 3, 433-446.

[14] Mikhailov B., Plasma gasification of coal, Thermal Plasma and new Materials Technology, ed. O.P. Solonenko, M. F. Zhukov, Vol. 2, Cambridge Interscience Publish., 1995, 345-369.

[15] Zasypkin I., M, Nozdrenko G. V., Production of acetylene and synthesis gas from coal by plasma chemical methods, Thermal plasma torches and Technologies, Vol. II., ed. O.P. Solonenko, Cambridge Interscience Publish., 2001, 234-243.
[16] Kezelis R., Mecius V., Valinciute V., Valincius V., Waste and biomass treatment employing plasma technology, J. of High Temp. Mat. Process. 8 (2004), 2, 273-282.
[17] Zhao ZL, Huang HT, Wu CZ, Li HB, Chen Y., Biomass pyrolysis in an argon/hydrogen plasma reactor, Chem. Engineering & Technology 24 (2001), 11, 197-199.
[18] W.R. Smith and R.W. Missen, Chemical Reaction Equilibrium Analysis (Wiley, New York, 1982).
[19] O. Coufal, Composition and Thermodynamic Properties of Thermal Plasma up to 50 kK, J. Phys. D: Appl. Phys. 40 (2007) 3371.
[20] O. Živný, Composition and Thermodynamic Functions of Non-ideal Plasma, Eur. Phys. J. D 54 (2009) 349.
[21] O. Coufal and O. Živný, Composition and Thermodynamic Properties of Thermal Plasma with Condensed Phases, Eur. Phys. J. D 61 (2011) 131.
[22] O. Coufal, P. Sezemský and O. Živný, Database System of Thermodynamic Properties of Individual Substances at High Temperatures, J. Phys. D: Appl. Phys. 38 (2005) 1265.
[23] M. Hrabovsky, M. Konrad, V. Kopecky, M. Hlina, Pyrolysis of wood in arc plasma for syngas production, Journal of High Temperature Material Processes **10** (4), 2006, pp. 557-570.
[24] M. Hlina, M. Hrabovsky, V. Kopecky, M. Konrad, T. Kavka, S. Skoblja, Plasma gasification of wood and production of gas with low content of tar, Czechoslovak Journal of Physics **56** (2006), Suppl. B, B1179-1184.
[25] P. Krenek, Thermophysical properties of H2O–Ar plasmas at temperatures 400–50,000 K and pressure 0.1 MPa, Plasma Chem. Plasma Process. **28** (2008), 107 - 122.
[26] P. Krenek, M. Hrabovsky, H_2O – Ar plasma property functions for modeling of hybrid water – gas plasma torch, Proc. of 18th Int. Symp. on Plasma Chemistry (ed. K Tachibana et al) , Kyoto, August 26-31, 2007, Book of Abstracts, 75, full paper on CD.
[27] Ansys Fluent® version 14.5 users guide